Interplanetary coronal mass ejection observed at STEREO-A, Mars, comet 67P/Churyumov-Gerasimenko, Saturn, and New Horizons en-route to Pluto. Comparison of its Forbush decreases at 1.4, 3.1 and 9.9 AU

O. Witasse[1], B. Sánchez-Cano[2], M. L. Mays[3], P. Kajdič[4], H. Opgenoorth[5], H. A. Elliott[6], I. G. Richardson[3,7], I. Zouganelis[8], J. Zender[1], R. F. Wimmer-Schweingruber[9], L. Turc[1], M. G. G. T. Taylor[1], E. Roussos[10], A. Rouillard[11], I. Richter[12], J. D. Richardson[13], R. Ramstad[14], G. Provan[2], A. Posner[15], J. J Plaut[16], D. Odstrcil[17], H. Nilsson[14], P. Niemenen[1], S.E. Milan[2], K. Mandt[6, 18], H. Lohf[9], M. Lester[2], J.-P. Lebreton[19], E. Kuulkers[1], N. Krupp[10], C. Koenders[12], M.K. James[2], D. Intzekara[8,1], M. Holmstrom[14], D. M. Hassler[20,21], B.E.S. Hall[2], J. Guo[9], R. Goldstein[6], C. Goetz[12], K.H. Glassmeier[12], V. Génot[11], H. Evans[1], J. Espley[22], N. J. T, Edberg[5], M. Dougherty[23], S. W. H. Cowley[2], J. Burch[6], E. Behar[14], S. Barabash[14], D. J. Andrews[5], N. Altobelli[8]

[1] European Space Agency, ESTEC, Keplerlaan 1, Noordwijk 2200 AG, The Netherlands.

[2] Radio and Space Plasma Physics Group, Department of Physics and Astronomy, University of Leicester, University Road, Leicester LE1 7RH, United Kingdom.

[3] Heliophysics Science Division, NASA Goddard Space Flight Center, Greenbelt, MD, USA

[4] Instituto de Geofísica, Universidad Nacional Autónoma de México, Ciudad de México, México.

[5] Swedish Institute of Space Physics, IRF, Uppsala, Sweden

[6] Southwest Research Institute, San Antonio, TX, USA

[7] Department of Astronomy, University of Maryland, College Park, MD 20742, USA

[8] European Space Agency, ESAC, Villanueva de la Cañada, Spain

[9] Institute of Experimental and Applied Physics, Christian-Albrechts-University, Kiel, Germany

[10] Max Planck Institute for Solar System Research Justus-von-Liebig-Weg, Göttingen, Germany

[11] IRAP, Toulouse, France

This article has been accepted for publication and undergone full peer review but has not been through the copyediting, typesetting, pagination and proofreading process which may lead to differences between this version and the Version of Record. Please cite this article as doi: 10.1002/2017JA023884

[12] Institute for Geophysics and extraterrestrial Physics, Technische Universität Braunschweig, Germany

[13] Center for Space Research, Massachusetts Institute of Technology Cambridge, USA

[14] Swedish Institute of Space Physics, IRF, Kiruna, Sweden

[15] NASA Headquarters, Science Mission Directorate, Washington, DC, USA

[16] Jet Propulsion Laboratory, Pasadena, CA, 91109, USA

[17] George Mason University, Fairfax, VA, USA

[18] Department of Physics and Astronomy, UTSA, San Antonio, TX, USA

[19] LPC2E, CNRS-Université d'Orléans, France

[20] Southwest Research Institute, Boulder, CO, USA

[21] Institut d'Astrophysique Spatiale, Orsay, France

[22] Laboratory for Planetary Magnetospheres, Goddard Space Flight Center, Greenbelt, MD, USA

[23] The Blackett Laboratory, Imperial College London, SW7 2BZ, United Kingdom.

Corresponding author: Olivier Witasse (owitasse@cosmos.esa.int)

Key Points:

- Study of the propagation of an ICME up to 111 AU
- Comparison of Forbush decreases triggered by the same ICME at 1.4, 3.1 and 9.9 AU
- Model-predicted ICME arrival times are in agreement with the observations
- An ICME disturbed the Solar wind during the Siding Spring comet flyby at Mars on 19 October 2014

Key Words:

- Interplanetary Coronal Mass Ejection, Forbush decrease, Mars, comet 67P, Saturn, New Horizons, Voyager 2

Abstract

We discuss observations of the journey throughout the Solar System of a large interplanetary coronal mass ejection (ICME) that was ejected at the Sun on 14 October 2014. The ICME hit Mars on 17 October, as observed by the Mars Express, MAVEN, Mars Odyssey and MSL missions, 44 hours before the encounter of the planet with the Siding-Spring comet, for which the space weather context is provided. It reached comet 67P/Churyumov-Gerasimenko, which was perfectly aligned with the Sun and Mars at 3.1 AU, as observed by Rosetta on 22 October. The ICME was also detected by STEREO-A on 16 October at 1 AU, and by Cassini in the solar wind around Saturn on the 12 November at 9.9 AU. Fortuitously, the New Horizons spacecraft was also aligned with the direction of the ICME at 31.6 AU. We investigate whether this ICME has a non-ambiguous signature at New Horizons. A potential detection of this ICME by Voyager-2 at 110-111 AU is also discussed. The multi-spacecraft observations allow the derivation of certain properties of the ICME, such as its large angular extension of at least 116°**,** its speed as a function of distance, and its magnetic field structure at four locations from 1 to 10 AU. Observations of the speed data allow two different solar wind propagation models to be validated. Finally, we compare the Forbush decreases (transient decreases followed by gradual recoveries in the galactic cosmic ray intensity) due to the passage of this ICME at Mars, comet 67P and Saturn.

1. Context

The study presented here was motivated by the analysis of Mars Express data acquired during the flyby of the Siding-Spring comet on 19 October 2014 [e.g. Svedhem et al., 2014; Gurnett et al., 2015]. A preliminary assessment of the Analyzer of Space Plasmas and Energetic Neutral Atoms (ASPERA-3) instrument on board Mars Express data showed that the Mars upper atmosphere was disturbed during that time, most likely due to a solar wind event, making the analysis of the comet-related effects more complex than anticipated. It was therefore decided to search for possible solar wind structures that could have been present at Mars during that period. An interesting and powerful coronal mass ejection (CME) candidate was found, which erupted from Solar Active Region 12192 on 14 October 2014 at around 18:30UT. The journey of this interplanetary CME (ICME) is studied in detail with in-situ data sets acquired by no less than eight spacecraft and one Mars rover. The ICME not only impacted the red planet, but also the STEREO-A spacecraft, comet 67P/Churyumov-Gerasimenko (comet 67P hereinafter), Saturn, and possibly New Horizons on its way to Pluto. The paper describes the propagation of this ICME out to 32 astronomical units (AU). In addition, Voyager-2 was near 111 AU travelling roughly in the same direction as New Horizons, and we investigate whether the ICME was also observed by this spacecraft in late March 2016.

Similar multi-spacecraft studies of ICME propagation have been recently published [e.g. Rouillard et al., 2010, Prise et al., 2015; Moestl et al., 2015] or indirectly inferred in the past by successive enhancements of the planetary auroral activity throughout the solar system [e.g. Prangé et al., 2004]. However, the propagation of Solar wind events in the outer heliosphere is still poorly understood. The originality of the present study resides in the good alignment of many spacecraft in the solar system with the direction of the ICME, allowing a comparison between observational data and propagation models. This gives us the opportunity to provide further insight into ICME propagation at large distances, such as the evolution of its magnetic structure or its speed profile. In addition, the observations provide an excellent opportunity to assess the effects of this ICME on planetary space weather, an emerging discipline [e.g. Plainaki et al, 2016; Lilensten et al., 2014].

The passage of an ICME may result in a sudden and steep depression in the intensity of Galactic cosmic rays (GCR). This phenomenon is called a “Forbush decrease” (FD), and is

typically measured by ground-based neutron monitors on Earth [e.g. Forbush, 1938; Cane, 2000]. Its importance here lies in the fact that it indirectly provides information about the propagation of ICMEs throughout the solar system, such as the magnetic field structure, the kinematic properties and the radial extent of the ICME. In this study, FDs generated by the passage of the ICME introduced above are identified at Mars, comet 67P, Saturn and Voyager 2. Comparison of their characteristics provides valuable information on the evolution of the ICME with heliocentric distance and its interaction with the Solar wind.

2. Propagation of the interplanetary coronal mass ejection: from the Sun to New Horizons

Figure 1 shows the positions of the planets on 14 October 2014, where the inner Solar system up to comet 67P is displayed in panel (a), the outer solar system up to Pluto orbit is in-panel (b), and the outer solar system up to the Voyager-2 position is in-panel (c). In this section, we first discuss a CME that was observed on this day. In each of the following subsections, we then assess whether the ICME associated with this CME hit several solar system bodies and spacecraft. The in-situ observations are described in each subsection, and the corresponding arrival times are provided in Table 1. Moreover, the predictions of two different solar wind propagation models are also given in Table 1 to support the data analysis. Finally, in order to simplify the text, each of the instruments used in this study is described briefly in the Appendix.

[FIGURE 1] [TABLE 1]

2.1. CME ejection

The 14 October 2014 CME was associated with an M1.1 (start time 18:21 UT) solar X-ray flare in active region 12192 located 13° below the solar equator that was closely followed by a long duration M2.2 (19:07 UT) flare from the same active region. Since the flares were still behind the east limb as seen from Earth, the X-rays were partially occulted. As Active Region 12192 rotated across the solar disk, it became the largest sunspot group observed in the last 24 years [Sun et al., 2015]. However, despite producing many major flares, this CME was the only large eruption originating from this active region, and for this reason it has been a topic of several studies [Thalmann et al., 2015; Sun et al., 2015; Yang et al., 2015]. Figure 2 summarizes several solar observations around the time of the CME. Figure 2a shows the solar disc at a wavelength of 131 angstrom as imaged by Solar Dynamics Observatory (SDO)

[Pesnell et al., 2012] Atmospheric Imaging Assembly (AIA) [Lemen et al., 2012] at 21:27 UT. The eruption seen above the east limb (left-hand part of the images) started at around 18:30 UT and was followed by bright post-eruption loops near the active region that continued to increase in height and persisted for more than a day, as discussed in detail by West and Seaton, [2015] using data from the Project for On Board Autonomy 2 (PROBA-2) satellite (Figure 2c). Figure 2f shows the Lyman-Alpha Radiation Monitor (LYRA) time-series observations from PROBA-2 using aluminum and zirconium filters, where the CME ejection on October 14 at 18:30 UT and an extended period with high level of irradiance in both filters is clearly observed. The CME was first observed at 18:48 UT on 14 October by the SOlar and Heliospheric Observatory (SOHO) [Domingo et al., 1995], Large Angle and Spectrometric Coronagraph Experiment (LASCO) [Brueckner et al., 1995]. Figure 2b shows an image from the C2 coronagraph at 20:48 UT, while Figure 2d shows an image of the Sun taken by STEREO-A SECCHI/EUVI at 21:39 UT. Note that the CME was ejected above the western limb (right-hand part of the images) as viewed from STEREO-A, located at 169° longitude (Heliocentric Earth Equatorial coordinates, HEEQ) in superior solar conjunction with respect to the Earth (see Figure 1). At this location, STEREO-A was working in a limited operational mode, and it was not possible to obtain a sequence of images covering the entire CME ejection. Nevertheless, a large post-eruptive loop system is present in the solar corona in the available images, which lasted for the next 48 h [West and Seaton, 2015]. This view from behind the Sun also allows us to further constrain the direction of the nose of the CME. Unfortunately, there are no observations from STEREO-B to help infer the CME trajectory because contact was lost with this spacecraft on October 1, 2014.

[FIGURE 2]

The Graduated Cylindrical Shell (GCS) [Thernisien et al., 2006; 2009] model was used to fit the 3D propagation of the CME using multipoint white light coronagraph observations from STEREO A and LASCO assuming a magnetic flux rope topology (Figure 2e). The three dimensional CME parameters were derived at a height of 21.5 $R_\odot$ (the inner boundary of the ENLIL model, to be discussed in section 2.2), specifically a speed of 850 ± 200 km/s, in a direction of -120° ± 30° longitude, and -11° ± 5° latitude and a full angular width of 106° ± 10°, all in HEEQ coordinates. The direction and width of the CME are represented by the dotted-dashed line sector in Figure 1.

2.2. Wang-Sheeley-Arge (WSA)-ENLIL+Cone model

To study the interplanetary propagation of this ICME, we use the Wang-Sheeley-Arge (WSA)-ENLIL+Cone model available from the Community Coordinated Modeling Center (CCMC). The global 3D MHD ENLIL model provides a time-dependent description of the background Solar wind plasma and magnetic field using the WSA coronal model [Arge and Pizzo, 2000; Arge et al., 2004] as input at an inner boundary of 21.5 solar radii ($R_\odot$) [Odstrcil et al., 1996; 2004; Odstrcil and Pizzo, 1999z; 1999b; Odstrcil, 2003]. A series of synoptic solar magnetic field maps derived from magnetograms are used as input to WSA-ENLIL as a basis for a time-dependent background Solar wind simulation. ENLIL version 2.8 was used in this work, with a time-dependent inner boundary constructed from a series of daily input WSA synoptic maps, each computed from a new Global Oscillation Network Group (GONG) [Harvey et al., 1996] daily synoptic "QuickReduce" magnetogram every 24 hours at the ENLIL inner boundary.

Generally, a CME disturbance is inserted in the WSA-ENLIL model as slices of a homogeneous spherical plasma cloud with uniform speed, density, and temperature as a time-dependent inner boundary condition at 21.5 $R_\odot$ with an unchanged background magnetic field. This modeling system does not simulate CME initiation, but uses kinematic properties of CMEs inferred from coronagraphs to model a CME-like hydrodynamic structure that simulates the effect of the pile-up of the plasma and magnetic field ahead of the CME, but not the effects of the CME flux-rope. The CME parameters used for the model input are as follows: radial speed 1015 km/s; longitude -150°; latitude -12°; full width 116°. These values were chosen from the range of GCS measurements that best reproduce in-situ observations. The parameters are within the error bar range of GCS measurements (section 2.1) and simulations initialized with these parameters produced output with a reasonable match to in-situ observations at Mars, STEREO A [Kaiser, 2005] and Rosetta [Glassmeier et al., 2007b].

For ICME propagation out to Saturn, a medium resolution (2°) simulation was performed on a spherical grid size of 1920 ×60 ×180 (r,θ,ϕ), with a range of 0.1 to 10.1 AU in radius (r), -60° to +60° in latitude (θ), and -180° to 180° in longitude (ϕ), all in HEEQ coordinates. The outer boundary was extended to include Pluto for an experimental low resolution (4°) simulation on a spherical grid size of 6720×20×90 (r,θ,ϕ), with a range of 0.1 to 35 AU in

radius (r), -40° to +40° in latitude (θ), and -180° to 180° in longitude (ϕ). The simulation period of 14 October 2014 to 14 April 2015 included 138 CMEs with speeds above 500 km/s and full angular widths above 50° from the web-accessible Database Of Notifications Knowledge Information (DONKI; https://kauai.ccmc.gsfc.nasa.gov/DONKI/), that is populated by CCMC's Space Weather Research Center (SWRC) team. The ENLIL model extended to 35 AU has not been modified to include the drag effect from pick-up ions or the enhancement of the wind mass density due to photoionization of neutral hydrogen entering the heliosphere from the interstellar medium, both of which play a role in ICME propagation at these distances. Figure 3 displays results of the simulation, in particular, the global heliospheric solar wind speed together with the magnetic field polarity and field lines, at the locations of interest for this study. ICMEs are outlined in black.

[FIGURE 3]

2.3. The CDPP propagation tool

In addition to the WSA-ENLIL+Cone model, the propagation of the ICME was assessed with the online tool developed by the Centre de Données de la Physique des Plasmas (CDPP propagation tool, http://propagationtool.cdpp.eu/). In this tool, the times of propagation between different points are based on simple analytic ballistic calculations combining a radial propagation [Rouillard et al, 2016] with the drag-based model [Vrsnak et al., 2013]. The propagation tool has been used in numerous studies to analyse solar wind structures and solar energetic particles (SEPs) in the inner heliosphere [Plotnikov et al., 2016; Rouillard et al., 2016; 2017; Sanchez-Diaz et al., 2017; Salas-Matamoros et al., 2016; Génot et al., 2014]. This article evaluates the accuracy of the tool for the first time in the outer heliosphere. The tool offers also visualisation of heliospheric imaging to evaluate the accuracy of the propagation model used. Unfortunately, in this case, the STEREO spacecraft were transiting behind the Sun at the time and did not record any solar wind images that could be exploited in this way. The tool was therefore run in its simplest mode with the following parameters (required by the on-line interface): start of the event on 14 October, 2014 at 18:30 UT; the source is at 230° (Carrington longitude); the Heliocentric Aries Ecliptic (HAE) longitude is 248.5°; the longitudinal extension of the CME is 116°, its initial speed is 880 km/s; the drag model uses a drag coefficient of 10^{-8} km^{-1}, consistent with [Cargill 2004; Vrsnak and Zic 2007], and a constant ambient Solar wind speed of 500 km/s, consistent with the WSA-

ENLIL+Cone solar wind simulation values. We note that this tool does not consider a variable ambient solar wind speed as input, but the results depends on a variable velocity with distance as a drag coefficient is included. Moreover, the motion of planets and probes along their orbits that may occur during the CME's propagation are accounted for in the derivation of impact times. Figure 4 shows a representation of the resulting ICME width and propagation direction up to 3 AU (Rosetta location) obtained with this tool. The rainbow-colored sector represents the propagation direction and extent of the ICME and is similar to the ENLIL result shown in Figure 1. The CDPP propagation tool and the WSA-ENLIL+Cone model used different speeds as inputs. These parameters were chosen to produce the best agreement with ICME arrival times but are within the error range of the GCS measurements (section 2.1).

[FIGURE 4]

2.4. STEREO-A and Venus

Figure 1 shows that STEREO-A and Venus were at similar longitudes, and hence might have been expected to have observed similar Solar wind structures related to the eastern flank of the ICME. The ICME-associated shock was observed at STEREO-A on 16 October 2014 at 20:15 UT. Figure 5 shows the STEREO-A beacon magnetic field data from IMPACT [Luhmann et al., 2008] and the solar wind proton speed, density and temperature from PLASTIC [Galvin et al., 2008]. During this time STEREO-A was in a lower telemetry state and the beacon data were written to the onboard recorder. These data were later downloaded in January 2016 when normal operations resumed, providing retrospective coverage of this period. The speed, density, temperature, and magnetic field strength all show the increases characteristic of a fast forward shock that arrived at 20:15 UT on October 16. There is evidence of an ICME with a magnetic cloud configuration [e.g., Klein and Burlaga, 1982] starting on 17 October at 20:00 UT (light gray shading). In particular, there are rotations in magnetic field components until around 19 October at 06:00 UT, with an average magnetic field magnitude of 15 nT and a maximum of 20 nT. The speed increased from around 300 km/s to 500 km/s on shock arrival and further increased, to ~650 km/s, in the sheath region (dark gray shading) between the shock and ICME. The magnetic field magnitude reached 35 nT in the sheath, and averaged 15 nT in the ICME, with a maximum of 20 nT. Observation of

magnetic cloud-like features near the expected flank of the ICME is perhaps surprising, and suggests that the ICME may have extended further to the east than suggested by modeling.

The shock and ICME might have been expected to have been detected earlier at the Venus Express spacecraft [Svedhem et al., 2009], which was in orbit around Venus from 2006 to January 2015. Unfortunately, the payload was switched off since this spacecraft was also in superior conjunction. Reviewing the housekeeping parameters, the star tracker background showed changes on 16 October around 7:00 UT. A star tracker can be overwhelmed by excessive proton radiation accelerated by an ICME-driven shock, so the background current, in case of large events, can be used as an indication of the passage of an ICME. However, it is not possible to conclude firmly that the changes in the Venus Express star tracker background were related to the passage of the shock of this ICME.

The WSA-ENLIL+Cone model output (Figure 3) indicates that the north-eastern portion of the ICME would have been expected to arrive at Venus at 09:00 UT on 16 October 2014 and at STEREO-A at 00:00 UT on 17 October 2014, while the CDPP propagation tool predicts an impact at Venus and Stereo-A at 07:12 UT and 20:57 UT respectively, on 16 October. Both model predictions agree reasonably well with the observed (October 16, 20:15 UT) arrival time of the shock at STEREO-A, with the WSA-ENLIL+Cone model predicting an arrival nearly four hours later than the actual arrival time, while the CDPP tool prediction was only 42 minutes behind. The changes in the Venus Express housekeeping parameters around 07:00 UT are also consistent with the predicted arrival times at Venus.

[FIGURE 5]

2.5. Mars

Figure 6 shows observations at Mars made by the Mars Express, MAVEN, and Mars Odyssey missions and by the Curiosity rover (Mars Science Laboratory (MSL) mission) on the Martian surface that are indicative of the arrival of the ICME and its associated shock on 17 October, 2014. In particular, panels a and b show the components and magnitude of the magnetic field respectively observed by MAVEN; the periodic intensity peaks correspond to the periapsis of its orbit. At 22:53:48 UT (indicated by the arrow), MAVEN was located in the magnetosheath of Mars near the terminator and detected a clear disturbance, whose

signatures include an enhancement of the magnetic field by a factor of 1.6 (from ~15 nT to ~25 nT) with respect to the previous magnetosheath orbit passage. There was also a substantial increase in the dynamic pressure in the Martian magnetosheath (Figure 6d) that lasted for at least 3 MAVEN orbits. Mars Express (MEX) was also located in the magnetosheath, further downstream from MAVEN, at this time. Despite the coarser temporal resolution of the Mars Express data, increases in the solar wind density by a factor of ~ 2, and the solar wind velocity from ~ 400 to ~700 km/s were clearly detected on 17 October (Figures 6e and 6f). However, it is difficult to discern the exact times of these changes because the ASPERA-3 instrument was not in operation for several minutes. Taken together, these changes are indicative of the arrival of the fast forward ICME-associated shock at Mars. Interplanetary shocks may accelerate energetic particles [e.g., Reames, 1999; Cane and Lario, 2006, and references therein], and indeed, the flux of shock-accelerated 30-1000 keV ions observed by the solar energetic particle instrument on MAVEN was significantly enhanced around the time of shock arrival (Figure 6c). In particular, the highest ion fluxes are reasonably consistent with the inferred arrival time of the shock. A typical, gradual decline over more than 3 days follows the shock. Other evidence of the arrival of the shock is the FD in the GCR fluxes evident in the observations from the Mars Odyssey HEND detector and the MSL-RAD instrument in Figures 6g and 6h. As noted above, FDs are frequently indicative of the passage of shocks and ICMEs and here, the onset of the decrease late on October 17 is consistent with the inferred arrival time of the shock at Mars. The ~20% decrease in the GCR signal during this FD was one of the deepest observed at Mars, and this suggests that the ICME as well as the shock may have encountered Mars, contributing to the FD. The FD will be discussed further in Section 3.

As mentioned in the first section, the analysis of the effects of the flyby of comet Siding-Spring on the Martian plasma system [Tricarito et al., 2014] was the original motivation for this study.

Closest approach of the comet to Mars occurred on October 19, only 44 hours after the main body of the ICME transited Mars. Thus, at the time of closest approach, the Martian plasma system was still recovering from the ICME impact, whilst the solar wind passing Mars remained significantly disturbed, as is evident in the SEP profiles, the Forbush decrease ending, and the elevated solar wind speeds. We can conclude that unfortunately, the influence of this ICME masked, to some extent, the comet flyby science. Despite this, Espley et al.

[2015] noted several magnetic signatures on October 19 that they attributed to the comet and not the ICME.

Regarding ICME propagation models, the CDPP tool predicts an impact at Mars at 22:51 UT on 17 October 2014, in almost perfect agreement with shock arrival time inferred from the MAVEN magnetometer measurements. The WSA-ENLIL+Cone model predicts an arrival time on 18 OCT 2014 at 0:00 UT, only 1 hour later than the observed arrival time. The middle-left panel of Figure 3 suggests that the far western flank of the ICME arrived at Mars within a high speed Solar wind stream.

[FIGURE 6]

2.6. Comet 67P/Churyumov-Gerasimenko

Figure 7 shows the magnetic field, radiation data and solar wind velocity measured by Rosetta at comet 67P at 3.1 AU from the Sun. Panels 7a and 7b show the magnetic field components and magnitude, respectively, as measured by the RPC-MAG [Glassmeier et al., 2007a] instrument onboard Rosetta. The magnetic field magnitude exhibits a sudden increase from 5 nT to 15 nT on 22 October at 16:30 UT when the ICME driven interplanetary shock arrived at the comet. At that time, the Rosetta spacecraft was in a terminator orbit at 10 km distance from the comet nucleus mass center, and the coma was relatively weak. Consistent with the arrival of the shock, Edberg et al. [2016] noted that a significant disturbance was observed in all the Rosetta plasma instruments, including a sudden signal increase in the ion and electron suprathermal sensor (~10-100 eV) of about one order of magnitude together with a general increase in energy of the electrons, and also a gradual increase of ~2 orders of magnitude in the ion composition analyzer Solar wind fluxes [see Figure 4 of Edberg et al., 2016]. Figure 7d shows an expanded view of the magnetic field observations around this feature. Interestingly, there is an indication in the magnetic field intensity of a second increase around an hour later that might be a further shock, making this a double shock suggestive of a merging of multiple structures. Moreover, the *By* component reached 30-40 nT and maintained this level for several hours. The shock and ICME arrival is also consistent with the FD observed in the radiation counts from around ~14:30 UT (Figures 7c and 7e) which reached a maximum decrease of 20% after 2 days. Finally, the proton speed (Figure 7f) exhibits a clear jump at 16:30 UT from 400 to 450 km/s, which is consistent with all the

previous observations. It was followed by a maximum speed of ~ 550 km/s about four hours later.

Edberg et al., [2016] have suggested that the signatures in Figure 7 might be interpreted as the ICME merging with a Stream Interaction Region (SIR). The WSA-ENLIL+Cone simulation (center right panel of Figure 3) indicates that the SIR was just ahead of the western flank of the ICME which was interacting with the trailing part of the high speed solar stream. Therefore, we expect the ICME to be entrained in the high speed stream. Figure 2e of Edberg et al. [2016] seems to support this interpretation. Observations shown in Figure 7 may indicate that the first jump in velocity and magnetic field at 16:30 UT could have been the forward SIR edge (or possibly the SIR driven shock) and the second jump at ~17:30 UT could have been the ICME still inside the SIR (or possibly the ICME driven shock). Moreover, the large FD in the observed by Rosetta (Figure 7c) suggests the passage of a large ICME, and in addition, as described later, the ICME also hit Saturn some weeks later. However, we note that a SIR also can produce a FD [e.g., Richardson, 2004]. Figure 7c indicates that the GCR decrease started before the large jump in magnetic field at ~17:30 UT. Therefore, it could be that the stream ahead of the shock/ICME produced the starting point of the decrease, and then, the ICME passage produced the deep decrease.

The arrival time predicted by the CDPP propagation tool is 17:00 UT on 22 October 2014, only half an hour later than the arrival time of the shock arrival obtained from the magnetometer and plasma data. The WSA-ENLIL+Cone model (centre-right panel of Figure 3) shows the far western flank of the ICME arriving at Rosetta on 22 October 2014 at 10:00 UT, a few hours earlier than the observed arrival.

[FIGURE 7]

2.7. Saturn

The ICME arrived at Saturn nearly one month after its eruption at the Sun, on the 12 November 2014. Providentially, the Cassini spacecraft was immersed in the Solar wind at this time, and the magnetometer [Dougherty et al., 2004] detected the arrival of the associated shock at 18:55 UT, as shown in Figures 8a and 8b, with an increase of the interplanetary magnetic field (IMF) strength from ~0.3 nT to 1.2 nT. This increase is significant, as the

typical IMF at Saturn is ~0.1 nT. From November 18 to 21, a well-defined region was observed that included a large rotation and enhancement in the magnetic field (up to 2 nT). We identify this structure with the ICME, which includes a clear magnetic cloud structure. It appears to resemble the "over-expanding" ICMEs, bounded by forward and reverse shocks, observed by the Ulysses spacecraft within the orbit of Jupiter [e.g., Gosling et al., 1998], though this cannot be confirmed with just the magnetic field observations. From November 22 to 28, the magnetic field remained at ~1 nT and then returned to more typical values of around 0.2-0.3 nT.

Passage of these structures was also evident in observations from other instruments on-board Cassini. In particular, a large FD (Figure 8c) was measured in the background of both the E4 and E6 channels of the LEEMS sensor [Krimigis et al., 2005] (the backgrounds are dominated by GCRs, but it is not possible to determine their energy), starting at the arrival of the shock. The declining phase of the FD lasted for ~5 days and two slopes are visible, between the shock and mid-day on November 15, and from that time to the maximum cosmic ray depression. As will be described in the next section, this change in slope is due to the transit of two different regions of the ICME (2-step FD). The first step on November 12-15, corresponds to the shock of the ICME structure. It was followed by a gradual decrease in the GCR due to the ICME sheath passage, which lasted for 3 days. The second step occurred on November 15-18 and coincided with the deepest point of the FD measured by LEMMS. In this case the FD slope is much steeper than in the previous case, and it is associated with the passage of the ejectas of the ICME as observed by the magnetometer and the LEMMS instrument (panel d). A rotation of the magnetic field structure of the ICME (Figure 8a and 8b) is detected, which also matches with the large increase in proton density of Figure 8d observed by LEMMS in the proton channel P2 (2280-4492 keV). From November 18 to 22, during the recovery phase of the FD, a large well-defined configuration is observed that corresponds to a large rotation and enhancement of the magnetic field (up to 2 nT). This structure is identified as the flux rope part of the ICME, called magnetic cloud. This structure could host high energy particles traveling together with the ICME structure, as observed in the small increase in the GCR from LEMMS. From November 22 to 28 the magnetic field remains at ~1 nT and goes back to normal conditions after that with an average magnetic field value of 0.2-0.3 nT. The recovery phase of the FD was longer than a month, suggesting that the shock and ICME modulated the GCR intensity over a wide region at the distance of Saturn. A very similar event at 1 AU was reported in Blanco et al. [2013], although the event

duration was different, presumably due to the different heliocentric distances of Saturn and Earth.

The arrival time of the shock at Saturn at 18:55 UT on the 12 November closely coincides with the predictions made by both model simulations. The CDPP propagation tool predicts an impact at Saturn at 16:09 UT on the 12 November 2014, only 2 hours and 46 min before the observed shock arrival. The WSA-ENLIL+Cone model predicts the arrival of the north and central portion of the ICME at 12:00 UT on November 15, and indicates that the ICME would take at least four days to transit Saturn. However, this is likely to be a minimum because the WSA-ENLIL+Cone model does not accurately model the structure of the ICME, and it is clear from Figure 8 that the time of passage was much longer than this estimate.

[FIGURE 8]

2.8. New Horizons

In October 2014, the New Horizons spacecraft was upstream of Pluto, prior to closest approach on 14 July, 2015 [Stern et al. 2015]. As discussed above, the ICME of interest in this paper passed Rosetta and since the Rosetta-Sun-New Horizons angle was only ~20° (Figure 1) the ICME may also have encountered New Horizons. Our first step was to estimate the time interval during which the ICME would reach New Horizons. We assumed that the ICME cannot travel faster than the mean velocity between Rosetta and Cassini (560 km/s, see Table 4) and also cannot travel slower than the lowest solar wind speed (~400 km/s) measured by New Horizons in early 2015 (see Figure 9, which shows solar wind parameters from the SWAP instrument [Elliott et al., 2016] including the energy per charge count rate spectrogram and the Solar wind speed, density and temperature, for the period 31 December 2014 to 15 March 2015). This leads to an interval of 18 January–14 February 2015 (DOY 18-45) in which to search for evidence of the ICME at New Horizons.

The identification of ICMEs in the New Horizons data is difficult because the state of an ICME at 30 AU is not well understood as only a few missions have transited to such large heliocentric distances. An ICME may maintain a distinct structure, as sometimes observed in the Voyager data [e.g. Wang and Richardson, 2004]; it may merge with other solar wind structures, or be worn down and blend in with the background wind. In our case, New

Horizons is at about 47° (or ~25 AU) from the center of the ICME. Therefore, if the spacecraft was hit by the ICME, it might have encountered its western flank where the signatures may be less distinct than nearer its "nose". In addition, there is no magnetometer aboard New Horizons, which makes ICME identification more difficult. In this study, solar wind data acquired with the SWAP instrument [Elliott et al., 2016] is used, as shown in Figure 9. The figure displays the energy per charge count rate spectrogram and the corresponding Solar wind proton speed, density, temperatures and dynamic pressure time series for the interval 31 December 2014 to 15 March 2015.

There are two possible scenarios: the ICME was eroded en route and blended into the background solar wind, such that no clear signature was observed in the New Horizons solar wind proton data, or the ICME missed New Horizons because the center was directed towards Saturn, 47° away from New Horizons in longitude and did not expand enough to hit the spacecraft. Since there is no magnetometer, we were not able to search for magnetic field rotations found in magnetic cloud flux ropes. This second scenario seems to be corroborated by the WSA-ENLIL+Cone simulation (Figure 3). The variability in the solar wind parameters is significantly reduced with increasing distance beyond 10 AU [Richardson et al., 2006; Elliott et al., 2016]. However, the signature of ICMEs, or a series of ICMEs, can at times be found at large distances as the Voyager and Pioneer missions have demonstrated [e.g. Wang and Richardson, 2001, 2004; Paularena et al., 2001; Richardson et al., 2002, 2006; Burlaga et al., 2005, 2007], and as auroral emissions at giant planets out to 20 AU have corroborated [e.g. Lamy et al., 2012]. On average, ICMEs expand by a factor of 5 in radial width between 1 and 10–15 AU and maintain a constant width as they move beyond 15 AU [Richardson et al., 2006]. At large distances in the outer heliosphere, ICMEs often form merged interaction regions (MIRs) [e.g. Burlaga et al., 1985, Le Roux and Fichtner, 1999]. MIRs are defined as regions of enhanced magnetic field and usually also have enhanced plasma speed and density; they have been observed in the heliosheath beyond 100 AU [e.g. Richardson et al., 2016]. In order to compare with New Horizons observations, a good example is the three ICMEs detection that Voyager 2 made in 1989 when it was transiting at about 28.2-29.3 AU from the Sun [Wang and Richardson, 2004], which is an analogous distance to New Horizons in this study. Wang and Richardson [2004] observed three structures with radial widths of 0.68-4.54 AU from observations of the helium abundance -an indicator of ICMEs- which are corroborated by magnetic field observations where clear magnetic field enhancements and component rotations (flux ropes) are found.

In Figure 9, there is a clear forward shock or wave that reached New Horizons on DOY 068. However, the enhanced solar wind speeds following the shock suggest that this shock reached New Horizons too late (with respect to the time window defined in the introduction of this section) to be associated with the ICME that previously encountered Venus, STEREO-A, Mars, comet 67P, and Saturn. Enhancements in the abundance of solar wind helium ions also characterize some ICMEs, but we do not see any dramatic enhancements in the amount of He^{++} in the ion spectrogram (Figure 9a). However, we do see a variety of short duration intervals where the proton temperature is slightly low, but we do not see any sustained low proton temperatures intervals. To determine if the temperatures were low, we compare the measured temperature to the expected temperature, as determined by using the solar wind speed and a formula derived by fitting a large data set of proton speed and temperature measurements [e.g. Elliott et al., 2005 and 2012]. The Solar wind temperature and speed are typically well correlated for both the fast and slow wind, but not during ICMEs where the temperature is lower than in the ambient Solar wind [Neugebauer and Snyder, 1966; Richardson and Cane, 1995; Elliott al, 2005]. The longest extended low temperature (Figure 9d) interval occurs prior to the 068 shock and extends for many days after that date, but as mentioned earlier, this shock occurs too late so it is unlikely to be related to the ICME of this study. We do see a distinct low density interval on days DOY 025-029. This low-density interval potentially could be an over-expanding interval or a large pressure balanced structure. To determine the type of structure (magnetic cloud for example) this low-density interval is, we would need magnetic field measurements which we do not have on New Horizons. On DOY 019 of 2015, there is a small rise in the speed from 400 to 430 km/s which is accompanied by a significant increase of ~30% in the proton density and in the temperature on the DOY 021, and of ~25% in the thermal and dynamic pressures on the same day. This enhancement is the largest one observed in the 4-month period of figure and the sign of a compression which could be associated with a SIR, MIR, or ICME sheath. As stated before, on DOY 025, a well-defined cavity is observed in the proton density and in both thermal and dynamic pressures. It is followed by another small rise in speed from 420 to 445 km/s. It coincides also with a drop in temperature that reaches a minimum value of 6000 K for a day, and after that, gradually increases until the second edge of the cavity where there was a sharp maximum of 40300 K, and then it goes back to the average temperature of 10500 K. In the absence of a magnetometer to corroborate this suggestion, we interpret these structures as a possible sign of the passage of an ICME. Solar wind proton density often has a

large enhancement ahead of the fast ICME ejecta as the density is piled-up by the motion of the ICME through the background wind, creating a sheath. Then, during the passage of an overexpanding ICME, the proton density and temperature tend to be relatively low as the magnetic pressure is dominant inside the structure. Therefore, a density cavity, like the one observed on DOY 025-029 by the SWAP instrument, is a possible indicator of an over expanding ICME or of a magnetic flux rope [e.g. Burlaga et al., 1981, 1982, 1987; Fuller et al., 2008; Byrne et al., 2010; Howard and DeForest, 2012; Webb and Howard, 2012; Manchester et al., 2014; Reisenfeld et al., 2003; Gosling et al., 1998].

This structure seems to be in agreement from a timing point of view with the arrival time of the ICME of this study at such distances. This arrival time is consistent with that from the CDPP propagation tool. On the other hand, the WSA-ENLIL+Cone simulation does not simulate the ICME passing New Horizons. However, if the ICME simulated by this latest model at 30 AU were a little larger in longitudinal width, the ICME would hit New Horizons on the 8 February 2015, ~15 days after the low-density cavity signature observed by New Horizons. We note again that the WSA-ENLIL+Cone extended to 35 AU does not account for the slowdown of the Solar wind as interstellar material is picked up. Therefore, this simulation should be taken as merely an indication in order to help in the ICME identification.

[FIGURE 9]

2.9. Voyager 2

As seen in Figure 1, if the ICME traveled by Pluto, there is the possibility that the ICME, or a MIR formed by this ICME, could have reached Voyager 2. This spacecraft is currently more than 110 AU from the Sun, within the heliosheath. Figure 10 displays Voyager 2 data from 2014 to mid-2016. Two MIRs are clearly identified, in mid-August 2015 and end-March 2016 (the latter is bracketed by the red vertical bars), from the variations of the dynamic pressure connected with a decrease of GCR. While the first MIR was observed too early to be associated with the ICME studied here, the second event is a plausible association. The arrival time at Voyager 2 is calculated following the same approach as in Liu et al. [2014]. We start from the possible event at New Horizons at the end of January 2015, and the Voyager 2 position in the range 110-111 AU. Then, assuming a constant speed of ~400±20 km/s up to the termination shock at ~82±2 AU, and 85±15% of this value after

this point [Liu et al, 2014], we estimated that the travel time was 375±47 days after leaving the Sun, leading to an arrival time at Voyager 2 between late December 2015 and late March 2016.

[FIGURE 10]

3. Forbush decreases detected at Mars, comet 67P and Saturn

A FD is a temporary reduction in the Galactic cosmic rays fluxes, typically with a sudden onset and rapid decrease followed by a more gradual recovery [Forbush, 1938]. FDs are now recognized as a consequence of the passage of ICMEs and their associated shocks-[e.g Cane, 2000 and references therein]. In particular, if the shock and ejecta are intercepted by an observer, a two-step decrease may be observed [e.g. Figure 1 of Richardson and Cane, 2011]. The first step occurs in the turbulent field region in the sheath following the shock; the resulting intensity-time profile is a linear decline during sheath passage followed by a recovery [e.g. Wibberenz et al., 1998]. The second step occurs with the arrival of the ICME. Minimum cosmic ray intensities are usually observed within this structure, due to the at least partially closed-field line geometry of the ICME as evidenced by the frequent presence of bi-directional suprathermal electron flows suggesting that magnetic field lines are rooted at the Sun at both ends [e.g., Gosling et al., 1987]. An extended recovery then occurs as the observer remains in the wake of the outward-propagating shock. As a result, the characteristic recovery time of a FD is larger for ICMEs associated with shocks. If the ICME alone is intercepted, but not the shock, then just the first step is observed followed by a recovery (Figure 1 of Richardson and Cane [2011]).

FDs have been observed in the outer Solar System by Ulysses, Pioneers 10 and 11, and Voyagers 1 and 2. For example, Bothmer et al. [1997] described several decreases of between 7 and 12% observed in June 1993 - February 1994 at 3.5-4.6 AU during the first solar orbit of Ulysses that could be associated with ICMEs previously detected moving out through the inner heliosphere. They concluded that the relatively weak shocks present did not strongly influence the GCR intensity, and minimum intensities were found inside the ICMEs. Moreover, short episodes of enhanced GCR intensity were observed inside the ICMEs at times when bidirectional suprathermal electron fluxes disappeared, suggesting that GCRs could favorably access the ICMEs along open magnetic field lines. Van Allen and Fillius

[1992] studied the propagation of an ICME that was launched on June 11, 1991 even further into the deep outer Solar System by analyzing the associated FDs observed at Earth, at 34 AU by Pioneer 11, at 53 AU by Pioneer 10 and most likely at 46 AU by Voyager 1. In this way, they inferred an apparent radial speed of 820 km/s that was independent of heliocentric distance, while the FD was found to have a similar size (~20 %) between 1 and 53 AU over a heliocentric ecliptic longitude extent of at least 173°. The recent systematic exploration of solar system bodies has enabled FDs to be studied more comprehensively at different heliocentric distances. For instance, FDs have been observed by the MSL mission both in transit to Mars [Zeitlin et al., 2013; Guo et al., 2015a], and on the Martian surface [Guo et al., 2015b], by Mars Odyssey [Zeitlin et al., 2010] in orbit at Mars, by Rosetta in orbit at comet 67P (this article), and by Cassini in orbit at Saturn [Roussos et al., 2011]. Thus although space weather is not the main objective of the instrumentation on these missions, changes in GCR rates associated with FDs constitute a powerful tool to identify Solar wind transient structures throughout the heliosphere.

Figure 11 displays the four FDs identified in this study at different locations in the Solar system associated with the same ICME. It is important to note here that the radiation monitors used in this study are not dedicated GCR sensors. Instead, changes in the background counts of these instruments due to the interaction of very energetic GCRs with the spacecraft/instrument (the GCR spectrum peaks at around ~ 1 GeV [e.g., Lockwood and Webber, 1996]) are used as proxies for the flux of GCRs. A summary of the timing of each decrease and a quantitative description of Figure 11 (top panel) are presented in Table 2. In order to compare the evolution of the FDs at Mars (1.4 AU), comet 67P (3.1 AU) and Saturn (9.9 AU), the decreases previously shown separately in Figures 6 to 8 have been plotted together in Figure 11 (top panel). The GCR intensity-time profiles have been aligned at the onset of each decrease, and the magnitudes have been normalized to the maximum intensity of each onset, to allow for the different sensors used in this study. We only show one channel for each instrument, although once normalized, every energy channel in SREM/Rosetta and in HEND/Mars Odyssey shows almost the same modulation, presumably because the backgrounds in each channel are due to GCRs penetrating the instruments. As a consequence, we consider that it is reasonable to compare the relative decrease, the duration of the FD and the slope of the decrease at different locations although we recognize that one should be cautious about reading too much into the FD sizes at different locations due to the different instruments used.

The red and green profiles (Figure 11a) denote the Martian data. We note that since the GCR intensity is only weakly attenuated in the Martian atmosphere, both MSL (green) and Mars Odyssey (red) recorded the FD [e.g. Guo et al., 2015b]. The onset in each case is identified as the instant when the largest decrease starts. This is most likely associated with shock passage. However, it is also evident that at Mars, there is a previous small decrease a day before the onset, suggesting that this may have been a 2-step decrease, in which case both a shock and ICME (associated with the larger second decrease) may have passed Mars. On the other hand, this early decrease is of similar size to the fluctuations seen generally in the data in Figure 11a, so this two-step interpretation is not conclusive.

At comet 67P (black profile), the possible 2-step signature is less obvious than at Mars. Since both bodies were perfectly aligned at that time (see Figure 1a), the same part of the ICME body is expected to have crossed both places. Therefore, if a shock (from the GCR point of view) is not observed at comet 67P, it could be for two reasons: the leading edge of the ICME disturbance has already interacted with the high speed stream and no longer has a clear shock, or the possible shock at Mars was an artifact of the natural variation of the data. Nevertheless, this possibility has been included in Table 2 for reference. What is clearly observed at comet 67P is a small precursor increase prior to the onset of the FD. This precursor enhancement is the result of a reflection of GCR particles from the main body of the ICME motion [e.g. Cane, 2000]. The onset for comet 67P has been considered to match the background level of GCR when the decrease starts, avoiding the previous small enhancement. Regarding Saturn, the FD (blue profile) is manifested with a different structure mainly due to two different reasons. The first is that Saturn is not aligned with Mars and comet 67P, being hit by a different part of the ICME structure (Saturn being close to the nose of the ICME). The second is that the heliocentric distance is much larger than at Mars and comet 67P, and, therefore, the transient structure should have been modified by the ICME expansion throughout the solar system. As mentioned in the previous section, two slopes are visible within the decrease in GCR as measured by Cassini. The first slope could be associated with the shock transit and the second with the ejecta. Since both steps in the decrease last for more than two days, we identify the onset of the profile (Figure 11a) with the starting point of the first-step decrease. As for the four profiles shown in this figure, the GCR intensity (y-axis) has been normalized with respect to the onset magnitude of each single event, such that only differences in the FD

due to the passage of the ICME are assessed, such as differences in the decrease intensity, in the slope of the decrease, or in the time of the recovery phase.

Figure 11a and Table 2 indicate that the closer to the Sun, the deeper, shorter and steeper the decreases are. These characteristics are associated with the nature of the ICME because the slope of the FD depends on its properties, such as the size of the magnetic structure, the intensity of the magnetic field or its radial extent [e.g. Cane et al., 1993; Blanco et al., 2013]. As expected, both Mars stations measure the same kind of decrease: FD duration, slope, and recovery time are in very good agreement. The only difference is the depth of the decrease, as MSL recorded a ~19% reduction in the GCR at the surface of the planet, and Mars Odyssey, based on neutron measurements, a ~23% reduction in orbit. These numbers should be seen as a lower limit, since the atmosphere changes the GCR spectra and has a cutoff energy for incoming particles. Focusing on Mars and comet 67P, which were perfectly aligned, the decrease depths are of the same order in both places (~17% measured by Rosetta and ~19% measured by the MSL). The main difference lies on the slope of the decrease, which is steeper at Mars. This is directly related to the longer duration of the decrease at comet 67P (~60h), nearly double the durations-at both Mars' stations (~35h). The variation in the slope of the decrease is directly associated with the decrease in speed of the ICME from 1.4 to 3.1 AU, as well as a larger radial extent. Regarding Saturn, some differences are observed. Saturn was impacted by the center of the ICME and a 2-step FD was measured due first to the shock and second to the ejecta. This is different from Mars and comet 67P which most probably only met the ejecta, or if there was a previous shock, it was travelling very close to the ICME body at both positions. Furthermore, the ICME arrived at Saturn about a month later. Therefore, the properties of the ICME could have changed at large solar distance, where the SIRs and the background solar wind are able to assimilate the ICMEs and erode them. Moreover, the magnetic field of the ICMEs tend to diminish with the distance due to the ICME expansion, resulting in a smaller FD in intensity. However, a very strong FD was observed by Cassini, which is the manifestation of a strong inner magnetic structure traveling with marked signatures. The decrease in depth (~15%) is slightly smaller than at Mars and comet 67P, most probably due to the previous explanation. A 15% decrease indicates a robust magnetic structure (flux rope) inside the ICME at the Saturn distance. The slope is clearly less steep, in agreement with a slower speed (see next section), and the recovery time is the longest, being about a month after the ICME transited the planet. Finally, a prolonged enhancement in the GCR background commenced several days before the decrease, is seen in

the four profiles. This enhancement is not due to the ICME propagation because as seen, for example in the case of Mars, this occurs before the ICME was launched. Therefore, it can be concluded that this peculiar characteristic is due to the solar wind modulation of the GCR and not to the ICME propagation because the same variations are seen at three different locations.

Finally, in order to confirm the link between this ICME and the FDs, we have checked the GCR measured at Earth's surface with the Bartol Neutron Monitor Network at eight different locations (Figure 11, bottom panel). None of these stations observed any kind of signal that could be associated with a FD, which indicates that the ICME did not reach Earth and also corroborates the fact that the decreases studied in this paper are associated with the ICME journey and not to another source.

[FIGURE 11] [TABLE 2]

4. ICME speed

The evolution of ICME propagation speeds with heliocentric distance is not well understood, in particular in the outer solar system. The dynamics of an ICME is determined by the Lorentz force, the gravitational force and drag forces due to the interaction of the ICME with the solar wind (e.g. Cargill 2004). The drag force can be considered as the predominant force affecting the propagation. As a result, the factors that affect the travel time are mostly the density, size, and initial speed of the ICME, and the difference between the ICME and ambient solar wind speed. In this study, the ICME propagation speeds have been obtained from in-situ measurements and from precise timing of between observations, and eventually compared to the simulations. Figure 12 shows the ICME speed as a function of radial distance, as extracted from the WSA-ENLIL+Cone simulation along three radial lines: one on the flank of the ICME reaching Mars, comet 67P and New Horizons at -86° longitude and 2° latitude (in red); the second on the flank reaching Venus and Stereo-A at 170° longitude and -6° latitude (in cyan); and the center of the ICME reaching Saturn at -174° longitude and -2° latitude (in black). The speed profiles exhibit a strong decrease from about 1000 to 580 km/s within 1.5 AU, followed by a gradual decrease down to about 450-500 km/s at ~15 AU. From there, the profiles are almost constant. The profile towards Mars (red line) does not decrease as fast because the western flank of the ICME was riding on a high-speed stream (Figure 3). Conversely, the STEREO-A/Venus profile (in blue) decreases faster because the eastern flank was in relatively slow solar wind. Figure 12 also shows the individual data

points of the ICME speed from in-situ measurements (symbols, see Table 3 for the values), together with the mean value of the speed obtained from the precise arrival times at each body (black horizontal lines, see Table 4 for the values). At STEREO-A, the ICME speed was measured by the PLASTIC instrument. At Mars, the ICME speed measurements were performed by ASPERA-3 on board Mars Express when it was transiting the Solar wind (Figure 6). At comet 67P, the ICME speed was derived from the analysis of ion counts recorded by the ICA sensor [Nilsson et al., 2007] in the RPC package on board Rosetta. The speed was derived from the energy of the proton spectra, and a maximum speed of about 550 km/s was determined (Figure 7). At Saturn, at the time of writing, no information about speeds is available. The Cassini instruments are not optimized for speed measurements in the solar wind, and estimation methods are still under development. The range of speeds shown for New Horizons corresponds to the Solar wind speeds observed in a window around the estimated arrival time. As mentioned in section 2.8, we did not identify any clear signature of a large ICME that had timing consistent with the inner heliospheric and solar observations. As seen in Figure 12, in general, spacecraft measurements agree well with the simulation, to within 50-100 km/s.

This is also seen in Table 3 which compares the in-situ ambient solar wind and ICME speeds, if observed, and the speed of the ICME in the WSA-ENLIL+Cone model. The ambient solar wind values were derived from the velocity profiles in Figures 5, 6, 7 and 9, just before each spacecraft was hit by the ICME. In-situ measurements indicate that the ICME speeds are always higher than the ambient solar wind speeds at 1, 1.4 and 3.1 AU. In particular, further from the Sun, the difference between the ICME and the ambient solar wind speeds decreases, in our case from 360 km/s at STEREO-A, ~150-200 km/s at Mars, and 150 km/s at comet 67P. This explains why the ICME decelerated most rapidly at small heliocentric distances. We note that at Mars and comet 67P, there was a high-speed stream present when the western flank of the ICME arrived, so at these locations, the ambient solar wind speed was obtained ahead of the fast stream. At 10 AU, the solar wind speeds from the WSA-ENLIL+Cone model reach ~ 500 km/s (Figure 3). Therefore, the inferred ICME speed seems to be approaching the background solar wind speed between 3 and 10 AU, consistent with the ICME speed decreasing due to the drag force until it eventually almost reaches the speed of the solar wind. At 31.5 AU, the solar wind profile shows only few small rises in velocity of ~50 km/s above the ambient speed which, as discussed in section 2.8, could be associated with the forward shock of ICMEs or MIRs.

[FIGURE 12] [TABLES 3 and 4]

5. Concluding remarks

In this study, we have analyzed the journey of an ICME and its respective passages past STEREO-A, Mars, comet 67P, and Saturn, which were clearly identified. The ICME must have hit Venus, although unfortunately the Venus Express payload was switched off due to the superior conjunction, the spacecraft engineering data do not show any obvious signal. Some signature of the ICME may also have been observed at Mercury (see the supplementary information), as indicated by the Messenger data.

We have attempted to follow the ICME travelling within the outer heliosphere well beyond Saturn and potentially hitting the New Horizons and Voyager 2 spacecraft. The identification of the ICME in the New Horizons data is not straightforward since there is no magnetometer, although we suggest that a cavity evident in the plasma data may be a signature of the ICME. The unclear and ambiguous identification could be due to the ICME being eroded on its flank, to being completely assimilated into the surrounding solar wind, or because the ICME missed New Horizons, as the WSA-ENLIL+Cone simulation suggests. A possible identification in the Voyager 2 data is proposed. All the events are simulated using the WSA-ENLIL+Cone solar wind model, which has been tuned specifically for this study to allow for a detailed modeling of the characteristics of this ICME. Its predictions on the arrival times throughout the solar system compare quite well with the observations. An excellent match is also found for arrival time estimates made using the on-line CDPP tool.

We are convinced that the observations spread in space and time are related to the same ICME, at least until 10 AU, for the following reasons. First, CME catalogues for the month of October 2014 indicate that there were no other large ICMEs propagating in the direction of Mars/Saturn/Pluto in that timeframe. Additionally, a unique time-dependent WSA-ENLIL+Cone simulation was performed in which 138 CMEs were included in the simulation interval of 6 months. The simulation results for other CMEs occurring near in time to the 14 October CME were carefully analyzed and determined not to have produced the ICME signatures of this study. Moreover, two propagation models were employed to compare the

observed ICMEs with the parent CME inserted into the models, and the excellent agreement between both models and the observed ICME arrival times gives confidence in this association. Finally, the almost perfect comparison of the Forbush decreases at Mars and at the comet 67P gives a complementary indication that the same ICME was detected at both places.

Summarizing the main advances of this study:

(1) Three main properties of the ICME and its propagation are derived in this study from the multi-spacecraft observations (that are not based only on data acquired at 1 AU, as is usually the case):

(a) The large angular extension (of at least 116 degrees) of the ICME, inferred from data acquired by spacecraft separated widely in longitude.

(b) The speed of the ICME as a function of heliocentric distance, including for the nose and for both flanks. The information on the speed comes from individual measurements (at Stereo-A, Mars, Rosetta and New Horizons), and also, from the precise timing of the ICME detection at every location.

(c) The magnetic field structure of the ICME at four different locations from 1 to 10 AU.

(2) The ICME speed data allow two different solar wind propagation models to be validated/calibrated.

(3) The comparison of Forbush decreases due to the same ICME at three locations widely separated in longitude and heliocentric distance is novel.

(4) The same ICME is tracked at six different Solar System locations at ~1, 1.4, 3, 10, 30 and 110 Astronomical Units, with data acquired by nine spacecraft. While there have been a few multi-spacecraft studies of ICMEs in the past, we do not believe that any have involved so many spacecraft over this range of distance. In addition, the use of so many spacecraft and instruments is not very usual in planetary sciences.

In addition, associating an ICME with its parent CME is not always straightforward, especially at large distances from the Sun. This becomes important when one wants to study the effects of ICMEs on planetary atmospheres. In this article, we show an excellent example

of how combining multiple spacecraft observations and modelling can lead to a plausible ICME-CME association out to at least 10 AU.

Also, this study provides the space weather context for a unique and important planetary event, the comet Siding Spring encounter with Mars. The ICME under study hit Mars about 44 hours before the closest approach of the comet to Mars. Although the Martian atmosphere might have been expected to have recovered from this impact during this interval, disturbances due to the ICME may have lasted longer, as is evident, for example, in the SEP profiles (Figure 6c). Thus, the interpretation of cometary particle effects on the Mars' atmosphere at the time of the Siding-Spring comet encounter should consider the lingering effects of the ICME passage. Models have shown that the cometary effects on the Martian atmosphere can be similar to those from extreme solar wind conditions or an ICME event [Wang et al., 2016].

Some lessons can be learned from this study: Three other spacecraft (Dawn, Venus Express and Spitzer) are likely to have been hit by this ICME based on the ENLIL model, although unfortunately no scientific data were available due to the fact that they were either not taking data during the cruise phase, behind the Sun, or not equipped for space weather studies. First, we emphasize the importance of a space weather monitoring package, including a magnetometer, to be embarked in all planetary and astronomical missions as a basic payload requirement. Secondly, it is recommended that plasma instruments continue to operate during solar superior conjunctions, even if only at a very low data rate, or continue to acquire data for later download.

Possible follow-up studies include detailed analysis of the ICME impact on the Mars and comet 67P plasma environments, and their comparison. Also, the New Horizons data could be revisited after a more thorough analysis of the whole solar wind data set has been made, and further updates to the numerical simulations of ICME propagation. More information on ICME properties can probably be obtained from a thorough review of these data sets. For example, we suspect that the evolution of the radial extension of the ICME could be inferred from the Forbush decrease data.

Acknowledgements

B.S-.C., G.P., S.E.M. M.L. M.K.J., S.W.H.C. and B.E.S.H acknowledge support through STFC grants ST/K001000/1, ST/N000749/1 and ST/K502121/1. M.L.M. and I.G.R. acknowledge the support of NASA LWS grants NNX15AB80G and NNG06EO90A, respectively. Simulation results have been provided by the Community Coordinated Modeling Center at the Goddard Space Flight Center through their public Runs on Request system (http://ccmc.gsfc.nasa.gov; run numbers Leila_Mays_092716_SH_1, Leila_Mays_100116_SH_1). The WSA model was developed by N. Arge at AFRL and the ENLIL Model was developed by D. Odstrcil at GMU. P.K.´s work has been supported by the PAPIIT grant IA104416. J.D.R. was supported by NASA's Voyager project. N.J.T.E. was funded by the Swedish National Space Board (135/13) and The Swedish Research Council (621-2013-4191). The Propagation Tool is designed and developed by the CDPP and GFI under CNES funding; it can be accessed from http://propagationtool.cdpp.eu/. All the MAVEN, MSL, Mars Odyssey, Cassini and New Horizons datasets are available at the NASA PDS. All the scientific data from Mars Express are available at the ESA PSA and AMDA (http://amda.cdpp.eu/). Rosetta scientific datasets are available at the ESA PSA and Rosetta SREM data at http://spitfire.estec.esa.int/sedat/dplot_odi.html. All the solar data are available at: https://sohodata.nascom.nasa.gov/cgi-bin/data_query, http://sdo.gsfc.nasa.gov/data/aiahmi/, https://stereo-ssc.nascom.nasa.gov/beacon/beacon_secchi.shtml, http://proba2.sidc.be/data/LYRA. Voyager 2 data are available at
http://web.mit.edu/space/www/voyager/voyager.html and
http://voyager.gsfc.nasa.gov/heliopause/data.html. The Bartol Research Institute neutron monitor program is supported by the United States National Science Foundation under grants PLR-1245939 and PLR-1341562, and by the University of Delaware Department of Physics and Astronomy and Bartol Research Institute, and can be downloaded from http://neutronm.bartol.udel.edu/ Very useful discussions within the Mars Upper Atmosphere Network (MUAN) and support from the ESA-ESTEC Faculty are acknowledged. Useful discussions with Michel Denis and Martin Shaw from ESA-ESOC, Christopher Tibbs and Oliver Jennrich from ESA-ESTEC, Jan-Uwe Ness from ESA-ESAC and Emilia Kilpua from University of Helsinki are acknowledged. We thank Toni Galvin from University of New Hampshire for useful discussion of the STEREO/PLASTIC data.

Appendix:

In this section, a brief description of the instrumentation used in this study is provided.

- **SOHO-LASCO (Figure 2):** The Large Angle and Spectrometric Coronagraph experiment (LASCO) on the Solar and Heliospheric Observatory (SOHO) spacecraft [Domingo et al., 1995]. It consists of three coronagraphs C1, C2, and C3, that together image the solar corona in visible light from 1.1 to 30 $R_{\odot}$ (C1: 1.1 – 3 $R_{\odot}$, C2: 1.5 – 6 $R_{\odot}$, and C3: 3.7 – 30 $R_{\odot}$) [Brueckner et al., 1995]. For this study, only C2 and C3 are used.

- **SDO-AIA (Figure 2):** The Atmospheric Imaging Assembly (AIA) of the Solar Dynamics Observatory (SDO) satellite views of the solar corona in X-rays, taking multiple simultaneous high resolution full-disk images of the corona and transition region up to 0.5 $R_{\odot}$ above the solar limb with 1.5-arcsec spatial resolution and 12 s temporal resolution [Lemen et al. 2012]. In this study, the AIA 131Å band is used, which is dominated by two Fe $_{VIII}$ lines at 130.94 and at 131.24 Å respectively. This band typically samples the flaring regions of the Sun's atmosphere.

- **STEREO-A – SECCHI EUVI (Figure 2):** The Extreme Ultraviolet Imager (EUVI) of the Sun Earth Connection Coronal and Heliospheric Investigation (SECCHI) is on board the STEREO-A spacecraft. Observations in the 195 Å bandpass, which is sensitive to the Fe XII ionization state of iron are used in this study.

- **PROBA-2 - SWAP (Figure 2)**: The Sun Watcher using Active Pixel System detector and Image Processing (SWAP) on board the Project for Onboard Autonomy 2 (PROBA-2) is a telescope that provides images of the solar corona at about 17.4 nm, a bandpass that corresponds to a temperature of roughly 1 million degrees, with a cadence of 1 image per 1-2 minutes, and field of view (FOV) of 54 arcmin.

- **PROBA-2 - LYRA (Figure 2)**: The Lyman-Alpha Radiation Monitor (LYRA) on board the Project for Onboard Autonomy 2 (PROBA-2) is a solar X and UV filter photometer [Dominique et al., 2013]. It monitors the solar irradiance in four passbands relevant to solar physics, space weather and aeronomy. This work has used

the aluminium filter channel (170-800 Å), which includes the He II line at 30.4 nm, and the zirconium filter channel (60-200 Å), which rejects the He II line.

- **STEREO-A – IMPACT/PLASTIC (Figure 5, 12):** STEREO-A beacon magnetic field data from In-situ Measurements of Particles and CME Transients (IMPACT) and Solar wind proton speed, density, and temperature from PLAsma and SupraThermal Ion Composition (PLASTIC). During the period of this study, STEREO-A was in a lower telemetry state and the beacon data were written to the onboard recorder. These data were later downloaded in January 2016 when normal operations resumed, providing retrospective coverage of this period.

- **VENUS EXPRESS - housekeeping data (Section 2.5):** Engineering data from Venus Express while the spacecraft was in solar superior conjunction. The data analyzed include star tracker background noise, spacecraft temperatures, etc.

- **MAVEN - MAG (Figure 6a, 6b, 6i):** The magnetic field instrument on board MAVEN consists of two fluxgate magnetometers that acquired data at 32 vector samples per second with a measured maximum of ±512 nT in the primary range (±2048 nT in the secondary range) giving it an approximate digital resolution of 8 pT [Connerney et al., 2015; Espley et al., 2015].

- **MAVEN - SEP (Figure 6c):** The Solar Energetic Particle Instrument (SEP) on board MAVEN consists of 2 sensors, each consisting of a pair of double-ended solid-state telescopes, measuring electrons and ions over the energy ranges ~30-1000 keV and ~30-12,000 keV/nuc respectively (only the ion flux of telescope 1 is used in this work). The SEP sensors are mounted on two corners of the top deck of the spacecraft positioned to ensure that the fields of view (FOVs) adequately cover the canonical Parker spiral direction (around which solar energetic particle distributions are typically centered) [MAVEN-SEP-technical note].

- **MAVEN - dynamic pressure (Figure 6d):** Key parameter from the MAVEN database. http://ppi.pds.nasa.gov/newrelease/datasetlist.jsp?id=65

- **MARS EXPRESS – ASPERA-3 (Figures 6e, 6f, 12):** Analyzer of Space Plasmas and Energetic Neutral Atoms (ASPERA-3) instrument [Barabash et al, 2006] on board Mars Express [Chicarro et al., 2004]. In this study, data from the ion mass analyzer (IMA) is used. The instrument samples ions across the energy range 10 eV/q – 30 keV/q, and is able to mass-resolve the main ion species within the Martian plasma environment (masses of 1, 2, 4, 16, and 32 amu/q). The energy resolution is 7% and the FOV is 90° (polar) x 360° (azimuth). Sampling across the polar FOV is broken into 16 elevation steps (-45deg to + 45deg), with a single step taking 12 s, and a full FOV scan taking 192 s.

- **MSL – RAD (Figures 6h, 11a):** The Radiation Assessment Detector (RAD) on board the Mars Science Laboratory (MSL) mission [Hassler et al., 2012] allows the identification of GCRs and SEPs that contribute to the radiation exposure on the surface of Mars. RAD provides differential fluxes in limited energy ranges, about 10–100 MeV/nuc for protons and helium, and integral fluxes of ions with higher energies in two different detectors. The RAD dynamic range covers the LET (the energy lost in an infinite volume of water) range from 0.2 to approximately 1000 keV/μm. RAD also measures neutrons and γ-rays with energies from ∼5 to 100 MeV. This study only shows data from the plastic scintillator detector.

- **Mars Odyssey – HEND (Figures 6g, 11a):** The High Energy Neutron Detector (HEND) [Boynton et al., 2004] on board the Mars Odyssey spacecraft allows the identification of GCRs and SEPs in orbit around Mars. The HEND instrument is composed of five separate sensors that provide measurements of neutrons in the energy range from 0.4 MeV up to 15 MeV [Zeitlin et al., 2010]. Two detectors are used in this work, the Outer Scintillator (an anti-coincidence detector) in channels 9-16 and the Medium Detector (MD) which is a 14-mm-thick moderator sensitive to neutrons. Both detectors provide information on minor to moderate solar particle events.

- **Rosetta - MAG (Figure 7a, 7b, 7d):** The magnetometer (MAG) on board Rosetta spacecraft is one of the 5 sensors that form the Rosetta Plasma Consortium (RPC) [Carr, C. et al., 2007]. It consists of two ultralight triaxial fluxgate magnetometer

sensors which mounted close to the tip of the 1.5 m long spacecraft boom and 15 cm closer to the spacecraft on the same boom [Glassmeier et al., 2007a].

- **Rosetta – ICA (Figure 7f, Figure 12)**: The Ion Composition Analyser (ICA) (Nilsson et al. 2007] is one of the five sensors that constitute the Rosetta Plasma Consortium (RPC) package on-board Rosetta spacecraft, and it is identical to the IMA instrument on board Mars Express. It measures the three-dimensional velocity distribution and mass distribution of positive ions.

- **Rosetta - SREM (Figure 7c, 7e, 11a):** The Standard Radiation Environment Monitor (SREM) on-board Rosetta is a solid state detector that measures both electrons with energies from 300 keV to 6 MeV and protons with energies from 10 to 300 MeV, and bins the measurements in overlapping energy channels [Mohammadzadeh et al., 2003]

- **CASSINI-Mag (Figure 8a, 8b, 8e):** The magnetometer on-board the Cassini spacecraft at Saturn consists of a fluxgate magnetometer operating at 32 vectors/sec [Dougherty et al., 2004]. 1 min averages are employed in this paper

- **CASSINI - LEMMS/MIMI (Figure 8c, 8d):** The Magnetosphere Imaging Instrument (MIMI) [Krimigis et al., 2004] on board Cassini is an instrument that detects energetic neutral and charged particles. MIMI consists of three different sensors, and in this study the dataset from the LEMMS (Low Energy Magnetospheric Measurement System) sensor is exploited. LEMMS's high energy telescope channels can respond to instrument penetrating GCR. In this study, we used channel E6 (energies between 1600 and 21000 keV) with data 1-hour averaged and with rates non-background subtracted. These channels are therefore MeV electron channels at a background level modulated by penetrating GCRs.

- **New Horizons - SWAP (Figure 9, 12):** Solar wind Around Pluto (SWAP) instrument on board New Horizons spacecraft. The SWAP instrument is a top-hat electrostatic analyzer (ESA) with a 10° by 276° FOV, and two Channel Electron Multiplier (CEM) detectors [McComas et al., 2008]. Analysis of the count rate energy distributions to

produce the Solar wind parameters used in this paper, is described by Elliott et al. [2016].

- **Voyager-2 – PLS (Figure 10):** The plasma experiment (PLS) consists of 4 Faraday cups, 3 of which look in the Solar wind direction, from which the plasma density, speed, temperature, and dynamic pressure, are derived.

- **Voyager-2 – CRS (Figure 10):** The Cosmic Ray Subsystem (CRS) instrument on board Voyager 2 provides GCR data for energies higher than 70 MeV.

- **Bartol Neutron Monitor Network (Figure 11b):** Bartol research Institute currently operates 8 neutron monitors placed on the surface of the Earth in order to form a complete picture of cosmic rays in space. The monitors are strategically located to provide precise, real-time, 3-dimensional measurements of the cosmic ray angular distribution.

- **MESSENGER – MAG (SI):** The Magnetometer (MAG) on the MErcury Surface, Space ENvironment, GEochemistry, and Ranging (MESSENGER) mission is a low-noise, tri-axial and fluxgate instrument. For Mercury operation, the resolution is 0.047-nT [Anderson et al., 2007].

References

Anderson, B.J., Acuña, M.H., Lohr, D.A. et al. Space Sci Rev (2007), The magnetometer instrument on MESSENGER, 131: 417. doi:10.1007/s11214-007-9246-7

Arge, C. N., and V.J. Pizzo, (2000), Improvement in the prediction of Solar wind conditions using near-real time solar magnetic field updates, Journal of Geophysical Research, 105, A5, 10,465-10,479.

Arge, C. N., J. G. Luhmann, D. Odstrčil, C.J. Schrijver, and Y. Li, (2004), Stream structure and coronal sources of the Solar wind during the May 12th, 1997 CME, JATP, 66, 1295

Baku, Coronal Mass Ejections from the Sun - Propagation and Near Earth Effects, PhD thesis. 2014

Barabash, S., et al. (2006), The Analyzer of Space Plasmas and Energetic Atoms (ASPERA-3) for the Mars Express Mission, Space Sci. Rev., 126, 113–164, doi:10.1007/s11214-006-9124-8.

Blanco et al., (2013), Observable Effects of Interplanetary Coronal Mass Ejections on Ground Level Neutron Monitor Count Rates, Solar Phys, 284:167–178, DOI 10.1007/s11207-013-0256-1

Bothmer, V., Heber, H., Kunow, H., Müller-Mellin, R., Wibberenz, G., Gosling, J. T., Balogh, A., Raviart, A., and Paizis, C.: 1997, 'The Effects of Coronal Mass Ejections on Galactic Cosmic Rays in the High Latitude Heliosphere: Observations from Ulysses' First Orbit', *Proc. 25th Int. Cosmic Ray Conf., Durban* 1, 333–336.

Boynton et al., (2004), The Mars Odyssey gamma-ray spectrometer instrument suite, *Space Science Reviews*, 110, 37–83, doi: 10.1007/978-0-306-48600-5_2

Brueckner, G. E et al., (1995), The Large Angle Spectroscopic Coronagraph (LASCO), Solar Physics, Volume 162, Issue 1-2, pp. 357-402, DOI: 10.1007/BF00733434.

Burlaga, L. F., E. Sittler, F. Mariani, and R. Schwenn (1981), Magnetic loop behind an interplanetary shock: Voyager, Helios, and IMP 8 observations, J. Geophys. Res., 86(A8), 6673–6684, doi:10.1029/JA86iA08p06673.

Burlaga, L. F., and K. W. Behannon (1982), Magnetic clouds: Voyager observations between 2 and 4 AU, Sol. Phys., 81, 181–192.

Burlaga, L.F., McDonald, F.B., Goldstein, M.L., Lazarus, A.J. (1985), Cosmic ray modulation and turbulent interaction regions near 11 AU. J. Geophys. Res. 90, 12,027–12,039.

Burlaga, L. F., K. W. Behannon, and L. Klein (1987), Compound streams, magnetic clouds and major geomagnetic storms, J. Geophys. Res., 92(A6), 5725–5734, doi:10.1029/JA092iA06p05725.

Burlaga, L.F., Ness, N.F., Stone, E.C., McDonald, F.B., Richardson, J.D. (2005), Voyager 2 observations related to the October–November 2003 solar events. Geophys. Res. Lett. 32, L03S05, doi:10.1029/2004GL021480.

Burlaga, L. F., N. F. Ness, and M. H. Acuña (2007), Magnetic fields in the heliosheath and distant heliosphere: Voyager 1 and 2 observations during 2005 and 2006, Astrophys. J., 668, 1246–1258, doi:10.1086/521349.

Byrne, J.P., S. A. Maloney, R.T.J. McAteer, J. M. Refojo and P.T. Gallagher, 2010, Propagation of an Earth-directed coronal mass ejection in three dimensions, Nature communications, 1:74, DOI: 10.1038/ncomms1077

Cane, H.V., Coronal Mass Ejections and Forbush Decreases, Space Science Reviews, 93, 55-77, 2000.

Cane, H. V., and D. Lario (2006), An introduction to CMEs and energetic particles, Space Sci. Rev., 123, 45–56, DOI: 10.1007/s11214-006-9011-3.

Cane, H. V., Richardson, I. G., and von Rosenvinge, T. T.: (1993), 'Cosmic Ray Decreases and Particle Acceleration in 1978–1982 and Associated Solar wind Structures', *J. Geophys. Res.* 98, 13 295–13 302.

Cargill, P., On the aerodynamic drag force acting on interplanetary coronal mass ejections, Solar Physics 221: 135–149, 2004.

Carr, C et al., RPC: The Rosetta Plasma Consortium, Space Sci. Rev., 128, 629–647, doi:10.1007/s11214-006-9136-4, 2007.

Chicarro, A., P. Martin, and R. Traunter (2004), Mars Express: A European mission to the red planet, European Space Agency Publication Division, SP-1240,pp. 3-16, Noordwijk, Netherlands.

Connerney, J. E. P., J. R. Espley, G. A. DiBraccio, J. R. Gruesbeck, R. J. Oliversen, D. L. Mitchell, J. Halekas, C. Mazelle, D. Brain, and B. M. Jakosky (2015), First results of the MAVEN magnetic field investigation, Geophys. Res. Lett., 42, doi:10.1002/2015GL065366.

Domingo, V., B. Fleck, and A. I. Poland (1995), The SOHO Mission: An overview, *Sol. Phys.*, *162*, 1–37, doi:10.1007/BF00733425.

Dominique, M.; Hochedez, J.-F.; Schmutz, W.; Dammasch, I. E.; Shapiro, A. I.; Kretzschmar, M.; Zhukov, A. N.; Gillotay, D.; Stockman, Y.; BenMoussa, A., (2013), The LYRA Instrument Onboard PROBA2: Description and In-Flight Performance, Solar Physics, 286, 1, 21-42, doi: 10.1007/s11207-013-0252-5

Dougherty M. K. et al., (2004), The Cassini Magnetic Field Investigation, Space Sci. Rev. 114, 331. DOI: 10.1007/s11214-004-1432-2

Edberg, N. J. T., A. I. Eriksson, E. Odelstad, E. Vigren, D. J. Andrews, F. Johansson, J. L. Burch, C. M. Carr, E. Cupido, K.-H. Glassmeier, *et al. (*2016*)*, Solar wind interaction with comet 67P: Impacts of corotating interaction regions, J. Geophys. Res. Space Physics, 121, 949–965, *doi:10.1002/2015JA022147.*

Elliott, H. A., D. J. McComas, N. A. Schwadron, J. T. Gosling, R. M. Skoug, G. Gloeckler, and T. H. Zurbuchen (2005), An improved expected temperature formula for identifying interplanetary coronal mass ejections, J. Geophys. Res., 110, A04103, doi:10.1029/2004JA010794.

Elliott, H. A., C. J. Henney, D. J. McComas, C. W. Smith, *and* B. J. Vasquez *(*2012*),* Temporal and radial variation of the solar wind temperature-speed relationship, J. Geophys. Res., 117, *A09102, doi:*10.1029/2011JA017125.

Elliott, H.A. et al., The New Horizons Solar wind Around Pluto (SWAP) Observations of the Solar wind from 11–33 au, The Astrophysical Journal Supplement Series, 2016

Espley, J. R., et al. (2015), A comet engulfs Mars: MAVEN observations of comet Siding Spring's influence on the Martian magnetosphere, Geophys. Res. Lett., 42, 8810–8818, doi:10.1002/2015GL066300.

Evans, H. D. R.; Bühler, P.; Hajdas, W.; Daly, E. J.; Nieminen, P.; Mohammadzadeh, A., Results from the ESA SREM monitors and comparison with existing radiation belt models, Advances in Space Research, Volume 42, Issue 9, p. 1527-1537, 2008

Forbush, S.E., (1938), On world-wide changes in cosmic-ray intensity, The Physical Review, 54, 12, 975-988.

Fuller, J., S. E. Gibson, G. de Toma, and Y. Fan, (2008) Observing the unobservable? modeling coronal cavity densities, The Astrophysical Journal, 678:515Y530.

Galvin A.B. et al., Space Sci Rev (2008) 136: 437–486 DOI 10.1007/s11214-007-9296-x

Génot, V.; André, N.; Rouillard, A.; Cecconi, B.; Lavraud, B.; Bourrel, N.; Budnik, E.; Bouchemit, M.; Gangloff, M.; Dufourg, N.; Beigbeder, L.; Modolo, R., Interplanetary shock detection and impact at planets : a science case for CDPP tools, European Planetary Science Congress 2014, EPSC Abstracts, Vol. 9, id. EPSC2014-684

Glassmeier et al., (2007a), RPC-MAG The Fluxgate Magnetometer in the ROSETTA Plasma Consortium, Space Science Reviews, 128: 649–670, DOI: 10.1007/s11214-006-9114-x

Glassmeier, KH., Boehnhardt, H., Koschny, D. et al. (2007b) The Rosetta Mission: Flying Towards the Origin of the Solar System, Space Sci Rev, 128, 1. doi:10.1007/s11214-006-9140-8

Gosling, J. T., D. N. Baker, S. J. Bame, W. C. Feldman, and R. D. Zwickl (1987), Bidirectional solar wind heat flux events, J. Geophys. Res., 92, 8519.

Gosling, J. T et al., Overexpanding coronal mass ejections at high heliographic latitudes : observations and simulations, JGR, 103, 1941, 1998

Guo, J. et al., (2015a), Variations of dose rate observed by MSL/RAD in transit to Mars, Astronomy & Astrophysics, 577, A58, DOI: 10.1051/0004-6361/201525680

Guo, J. et al., (2015b), Modeling the Variations of Dose Rate Measured by RAD during the First MSL Martian Year: 2012–2014, The Astrophysical Journal 810, 1, 24.doi: 10.1088/0004-637X/810/1/24

Gurnett et al., (2015), An ionized layer in the upper atmosphere of Mars caused by dust impacts from comet Siding Spring, Geophysical Research Letters, Volume 42, Issue 12, pp. 4745-4751.

Harvey, J.W., F. Hill, R. P. Hubbard, J. R. Kennedy, J. W. Leibacher, J. A. Pintar, P. A. Gilman, R. W. Noyes, A. M. Title, J. Toomre, R. K. Ulrich, A. Bhatnagar, J. A. Kennewell, W. Marquette, J. Patrón, O. Saá and E. Yasukawa, (1996), The Global Oscillation Network Group (GONG) Project, *Science,* Vol. 272, Issue 5266, pp. 1284-1286 DOI: 10.1126/science.272.5266.1284

Hassler, D.M., C.Z. Zeitlin, R.F. Wimmer---Schweingruber, S. Bottcher, C. Martin, J. Andrews, E. Bohm, D. Brinza, M. Bullock, S. Burmeister, B. Ehresmann, M. Epperly, D. Grinspoon, J. K¨ohler, O. Kortmann, K. Neal, J. Peterson, A. Posner, S. Rafkin, L. Seimetz,

K. Smith, Y. Tyler, G. Weigle, G. Reitz, and F. Cucinotta, (2012), The Radiation Assessment Detector (RAD) Investigation, Space Science Reviews, 170, Issue 1-4, pp. 503-558.

Howard, T.A., and C. E. DeForest, Inner heliospheric flux rope evolution via imaging of coronal mass ejections, The Astrophysical Journal, 746:64 (12pp), doi:10.1088/0004-637X/746/1/64

Kaiser, M. L., The STEREO mission: an overview, Advances in Space Research, Volume 36, Issue 8, p. 1483-1488, 2005

Klein, L. W., and Burlaga, L. F., Interplanetary magnetic clouds at 1 AU, Journal of Geophysical Research, vol. 87, Feb. 1, 1982, p. 613-624

Krimigis, S. et al., Magnetosphere Imaging Instrument (MIMI) on the Cassini Mission to Saturn/Titan, Space Science Reviews, Volume 114, Issue 1-4, pp. 233-329, 2005

Lamy, L., et al. (2012), Earth-based detection of Uranus' aurorae, Geophys. Res. Lett., 39, L07105, doi:10.1029/2012GL051312.

Lawrence, D. J., P. N. Peplowski, W. C. Feldman, N. A. Schwadron, and H. E. Spence (2016), Galactic cosmic ray variations in the inner heliosphere from solar distances less than 0.5 AU: Measurements from the MESSENGER Neutron Spectrometer, J. Geophys. Res. Space Physics, 121, doi:10.1002/2016JA022962

Lemen, J. R., et al. (2012), The Atmospheric Imaging Assembly (AIA) on the Solar Dynamics Observatory (SDO), *Sol. Phys.*, *275*, 17–40, doi:10.1007/s11207-011-9776-8.

Le Roux., J. A., and H. Fichtner, (1999), Global merged interaction regions, the Heliospheric termination shock, and time-dependent cosmic ray Modulation, JOURNAL OF GEOPHYSICAL RESEARCH, VOL. 104, NO. A3, PAGES 4709-4730, MARCH 1, 1999

Lilensten, J., A.J. Coates, V. Dehant, T. Dudok de Wit, R.B. Horne, F. Leblanc, J. Luhmann, E. Woodfield, and M. Barthélemy. What characterizes planetary space weather? Astron. Astrophys. Rev., 22–79, 2014, DOI: 10.1007/s00159-014-0079-6.

Liu, Y. D., Richardson, J. D., Wang, C. & Luhmann, J. G. Propagation of the 2012 March Coronal Mass Ejections from the Sun to Heliopause, 2014, ApJ788, L28

Lockwood, J. A., (1971). Forbush Decreases in the Cosmic Radiation, Space Science Reviews, 12, 5, 658-715.

Lockwood, J. A., and W. R. Webber (1996), Comparison of the rigidity dependence of the 11-year cosmic ray variation at the earth in two solar cycles of opposite magnetic polarity, J. Geophys. Res., 101(A10), 21573–21580, doi:10.1029/96JA01821.

McComas, D. et al. (2008), The Solar wind Around Pluto (SWAP) Instrument Aboard New Horizons, *Space Sci Rev, 140*(1), 261–313, doi:10.1007/s11214-007-9205-3

Luhmann J.G. et al., 2008, SSRv (2008) 136: 117–184 , DOI 10.1007/s11214-007-9170-x

Manchester, W. B., IV, J. U. Kozyra, S. T. Lepri, and B. Lavraud (2014), Simulation of magnetic cloud erosion during propagation, J. Geophys. Res. Space Physics, 119, 5449–5464, doi:10.1002/2014JA019882.

Moestl, C. et al. Strong coronal channelling and interplanetary evolution of a solar storm up to Earth and Mars. Nat. Commun. 6:7135 doi: 10.1038/ncomms8135 (2015).

Mohammadzadeh, A., H. Evans, P. Nieminen, E. Daly, P. Vuilleumier, P. Bühler, C. Eggel, W. Hajdas, N. Schlumpf, A. Zehnder, J. Schmeider, R. Fear, (2003), The ESA Standard Radiation Environment Monitor Program: first results from PROBA-1 and INTEGRAL. IEEE Trans. Nucl. Sci. 50 (6), 2272–2277, doi: 10.1109/TNS.2003.821796

Neugebauer, M. and Snyder, C. W., Mariner 2 Observations of the Solar Wind, 1, Average Properties, Journal of Geophysical Research, Vol. 71, p.4469, 1966

Nilsson, H., et al., RPC-ICA: The Ion Composition Analyzer of the Rosetta Plasma Consortium, Space Science Reviews, Volume 128, Issue 1-4, pp. 671-695, 2007

Odstrcil, D., Z. Smith and M. Dryer, (1996), Distortion of the heliospheric plasma sheet by interplanetary shocks, *Geophys. Res. Lett*., 23, 2521 - 2524. doi:10.1029/96GL00159.

Odstrcil, D., and V.J. Pizzo, (1999a), Three-dimensional propagation of CMEs in a structured Solar wind flow: 1. CME launched within the streamer belt, *J. Geophys. Res*., 104, 483 – 492, doi:10.1029/1998JA900019.

Odstrcil, D., and V.J. Pizzo, (1999b), Three-dimensional propagation of coronal mass ejections in a structured Solar wind flow 2. CME launched adjacent to the streamer belt, *J. Geophys. Res*., 104, 493 – 504, doi:10.1029/1998JA900038.

Odstrcil, D., (2003), Modeling 3-D Solar wind structure, Advances in Space Research, 32, 497 – 506, doi:10.1016/S0273-1177(03)00332-6.

Odstrcil, D., P. Riley and X.P. Zhao, (2004), Numerical simulation of the 12 May 1997 interplanetary CME event, *J. Geophys. Res*., 109, 2116, doi:10.1029/2003JA010135.

Paularena, K. I., C. Wang, R. von Steiger, and B. Heber (2001), An ICME observed by Voyager 2 at 58 AU and by Ulysses at 5 AU, Geophys. Res. Lett., 28, 2753.

Pesnell, W. D., B. J. Thompson, and P. C. Chamberlin, (2012) *The Solar Dynamics Observatory (SDO)*, Solar Physics, doi: 10.1007/s11207-011-9841-3.

Plainaki C, Lilensten J, Radioti A, Andriopoulou M, Milillo A, et al. Planetary space weather: scientific aspects and future perspectives. J. Space Weather Space Clim., 6, A31, 2016, DOI: 10.1051/swsc/2016024.

Plotnikov,I., et al., Long-Term Tracking of Corotating Density Structures Using Heliospheric Imaging, Solar Physics, Volume 291, Issue 6, pp.1853-1875, 2016

Prangé et al., Nature, Volume 432, Issue 7013, pp. 78-81 (2004).

Prise, A. J., L. K. Harra, S. A. Matthews, C. S. Arridge, and N. Achilleos (2015), Analysis of a coronal mass ejection and corotating interaction region as they travel from the Sun passing Venus, Earth, Mars, and Saturn, J. Geophys. Res. Space Physics, 120, 1566–1588, doi:10.1002/2014JA020256.

Reames, D. V. (1999), Particle acceleration at the Sun and in the heliosphere, Space Sci. Rev. 90, 413–491, DOI:10.1023/A:1005105831781.

Reisenfeld, D.B. et al. (2003), Properties of high-latitude CME-driven disturbances during Ulysses second northern polar passage, GRL, VOL. 30, NO. 19, 8031, doi:10.1029/2003GL017155

Richardson I.G. (2004), Energetic particles and corotating interaction region in the solar wind, Space Sci. Rev., 111: 267–376, 2004

Richardson, I.G., and Cane, H.V., (2005), Regions of abnormally low proton temperature in the solar wind (1965-1991) and their association with ejecta, Journal of Geophysical Research, Volume 100, Issue A12, p. 23397-23412

Richardson, I.G., and Cane, H.V., (2011), Galactic Cosmic Ray Intensity Response to Interplanetary Coronal Mass Ejections/Magnetic Clouds in 1995 – 2009, Solar Phys, 270:609-627, doi: DOI 10.1007/s11207-011-9774-x

Richardson, J. D., K. I. Paularena, C. Wang, and L. F. Burlaga (2002), The life of a CME and the development of a MIR: From the Sun to 58 AU, J. Geophys. Res., 107(A4), 1041, doi:10.1029/2001JA000175.

Richardson, J.D., Y. Liu, C. Wang, L.F. Burlaga, (2006), ICMES at very large distances, Advances in Space Research, 38, 528–534, doi:10.1016/j.asr.2005.06.049

Richardson, J.D., et al., Voyager Observations of Magnetic Sectors and Heliospheric Current Sheet Crossings in the Outer Heliosphere, The Astrophysical Journal, Volume 831, Issue 2, article id. 115, 6 pp. (2016).

Rouillard, A., et al., Deriving the properties of coronal pressure fronts in 3-D: application to the 17 May 2012 ground level enhancement, eprint arXiv:1605.05208, 2016

Rouillard, A.P., Lavraud, B., Genot, V., Bouchemit,M., et al., A propagation tool to track solar wind structures in the heliosphere, submitted to Planetary Space Weather, 2017

Roussos et al., (2011), Long- and short-term variability of Saturn's ionic radiation belts, Journal of Geophysical Research, Volume 116, Issue A2, CiteID A02217.

Salas-Matamoros, C. et al., Coronal mass ejection-related particle acceleration regions during a simple eruptive event, Astronomy & Astrophysics, Volume 590, id.A135, 2016

Sanchez-Diaz, E. Rouillard, A.P., Davies, J.A., Lavraud, B., Sheeley, N.R., Pinto, R.F., Kilpua, E., Plotnikov, I., Genot, V., Formation of blobs, in Revision, ApJ Letters, 2017

Stern, A. et al., The Pluto system: Initial results from its exploration by New Horizons, Science, Volume 350, Issue 6258, id.aad1815 (2015)

Sun, X., Bobra, M.G., Hoeksema, J.T., Liu, Y., Li, Y., Shen, C., Couvidat, S., Norton, A.A. and Fisher, G.H., (2015), Why is the great solar active region 12192 flare-rich but CME-poor?, *The Astrophysical Journal Letters*, 804, L28, doi:10.1088/2041-8205/804/2/L28

Svedhem et al., Venus Express mission, Journal of Geophysical Research, Volume 114, CiteID E00B33, 2009

Svedhem et al., (2014), Mars Express Observations During Comet Siding Spring Mars Encounter, American Geophysical Union, Fall Meeting 2014, abstract #P42A-03

Thalmann, J. K., Y. Su, M. Temmer, and A. M. Veronig, (2015), The confined X-class flares of solar active region 2192, *The Astrophysical Journal Letters*, 801, L23, doi:10.1088/2041-8205/801/2/L23

Thernisien, A.F.R., Howard, R.A., Vourlidas, A.: 2006, Modeling of flux rope coronal mass ejections. *Astrophys. J.* 652, 763 – 773. doi:10.1086/508254.

Thernisien, A., A. Vourlidas, and R.A. Howard, (2009), Forward Modeling of Coronal Mass Ejections Using STEREO/SECCHI Data, Sol Phys, 256:111. doi:10.1007/s11207-009-9346-5.

Tricarito, P., et al., Delivery of Dust Grains from Comet C/2013 A1 (Siding Spring) to Mars, The Astrophysical Journal Letters, Volume 787, Issue 2, article id. L35, 5 pp. (2014).

Van Allen, J.A., and R.W. Fillius, (1992), Propagation of a large Forbush Decrease in cosmic-ray intensity past the Earth, Pioneer 11 at 34 AU, and Pioneer 10 at 153 AU, Geophysical Research Letter, 19, 14.

B. Vršnak, T. Žic, D. Vrbanec, M. Temmer, T. Rollett, C. Möstl, A. Veronig, J. Čalogović, M. Dumbović, S. Lulić, Y.-J. Moon, and A. Shanmugaraju. Propagation of Interplanetary Coronal Mass Ejections: The Drag-Based Model. Solar Phys., 285:295-315, July 2013.

Wang, C., and J. D. Richardson (2001), Voyager 2 observations of helium abundance enhancements from 1 – 60 AU, J. Geophys. Res., 106, 5683.

Wang, C., and J. D. Richardson (2004), Interplanetary coronal mass ejections observed by Voyager 2 between 1 and 30 AU, J. Geophys. Res., 109, A06104, doi:10.1029/2004JA010379

Wang, et al., (2016), Cometary sputtering of the Martian atmosphere during the Siding Spring encounter, Icarus, Volume 272, 301–308, doi: http://dx.doi.org/10.1016/j.icarus.2016.02.040

Wang and Richardson, Interplanetary coronal mass ejections observed by Voyager 2 between 1 and 30 AU, JGR 2004

Webb, D.F. and T.A. Howard, (2012), Coronal Mass Ejections: Observations, Living Rev. Solar Phys., 9, 3, http://www.livingreviews.org/lrsp-2012-3

Vrsnak, B. and Zic, T., Transit times of interplanetary coronal mass ejections and the solar wind speed, Astronomy and Astrophysics, Volume 472, Issue 3, September IV 2007, pp.937-943, 2007

West, M.J. and D.B. Seaton, (2015), SWAP observations of post-flare giant arches in the long-duration 2014 October 14 solar eruption, *The Astrophysical Journal Letters*, 801, L6, doi:10.1088/2041-8205/801/1/L6

Wibberenz, G., J. le Roux, M. Potgieter, M. et al. (1998), Transient effects and disturbed conditions, Space Science Reviews, 83, 309. doi:10.1023/A:1005083109827

Winslow, R. M., B. J. Anderson, C. L. Johnson, J. A. Slavin, H. Korth, M. E. Purucker, D. N. Baker, and S. C. Solomon (2013), Mercury's magnetopause and bow shock from MESSENGER Magnetometer observations, J. Geophys. Res. Space Physics, 118, 2213–2227, doi:10.1002/jgra.50237.

Yang, S., J. Zhang, F. Jiang, and Y. Xiang, (2015), Oscillating light wall above a sunspot light bridge, *The Astrophysical Journal Letters*, 804, L27, doi:10.1088/2041-8205/804/2/L27

Zeitlin et al., (2010), Mars Odyssey measurements of Galactic cosmic rays and solar particles in Mars orbit, 2002–2008, SPACE WEATHER, VOL. 8, S00E06, doi:10.1029/2009SW000563

Zeitlin et al., (2013), Measurements of Energetic Particle Radiation in Transit to Mars on the Mars Science Laboratory, Science, 340, 10.1126/science.1235989

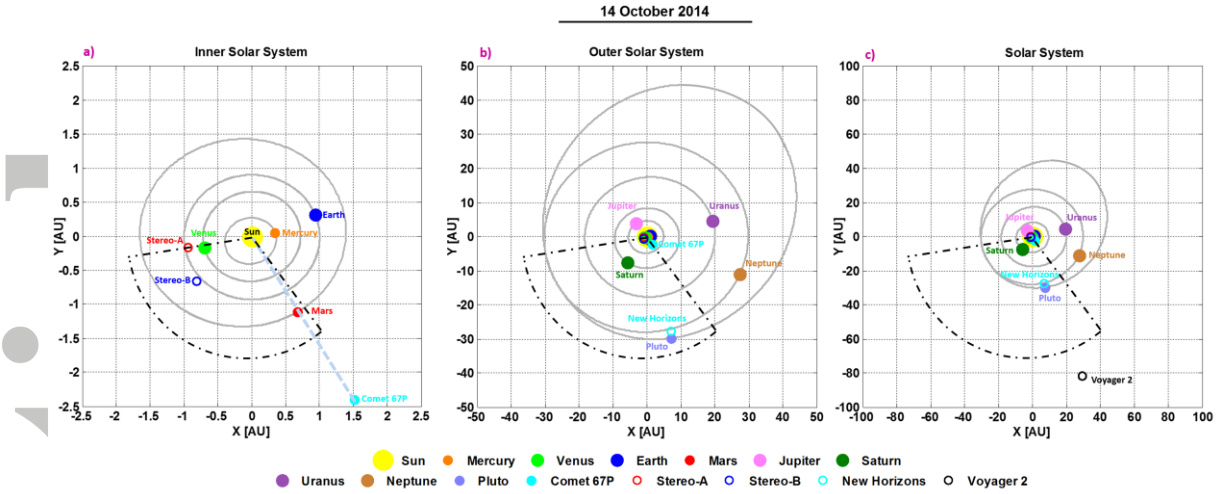

Figure 1: Planet positions on 14 October 2014. Panel a: Inner solar system out to comet 67P position. Panel b: Outer solar system out to Pluto orbit. Panel c: Full solar system out to Voyager 2 position. In all the panels, the reference frame is J2000. Planets are identified in the legend and with a label in each panel, the gray lines indicate the orbit of each planet, the dashed-dotted blue line highlights the alignment of Mars and comet 67P, and the dashed-dotted black sector indicates the width of the ICME with respect to the solar system. The ICME did not hit Earth. Around the CME ejection time, Venus was at 0.72 AU from the Sun, at 174° longitude, -3.3° latitude. STEREO-A was at 0.96 AU from the Sun, at 169° longitude, -6.2° latitude. Mars was at 1.4 AU from the Sun, -82° longitude, 3.3° latitude. On 22 October 2014, Rosetta was at 3.1 AU from the Sun, -88° longitude, -1.5° of latitude. On the 12 November 2014, Cassini was at 9.9 AU from the Sun, -174° longitude, -0.3° of latitude. In late January 2015, New Horizons was at 31.5 AU from the Sun, and -117° longitude, 5.3° of latitude. All the coordinates are given in the Heliocentric Earth Equatorial (HEEQ) reference system.

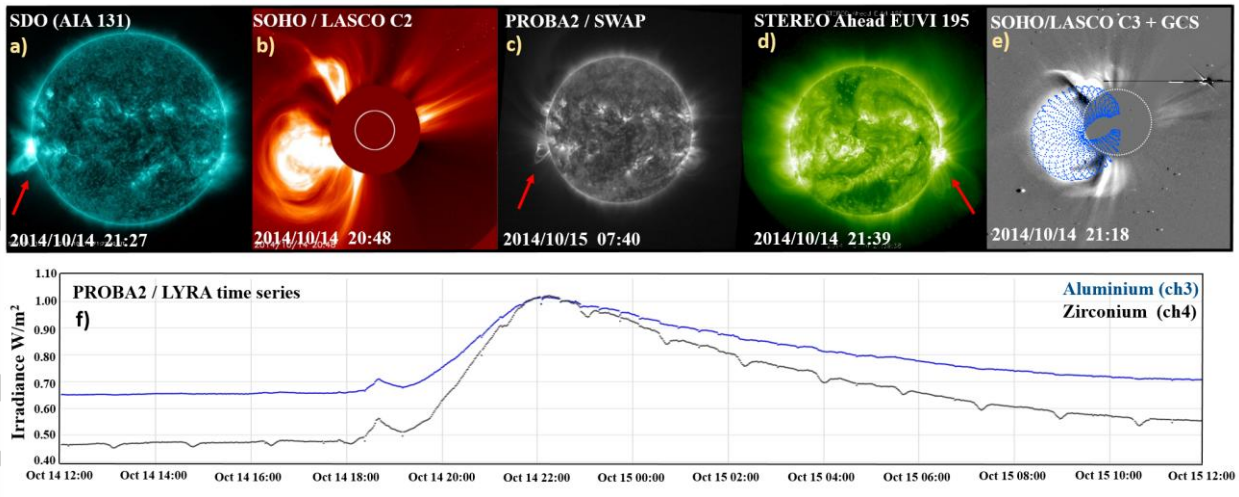

Figure 2: CME ejected on 14 October 2014 at ~18:30 UT. Panel a: SDO AIA image taken at 21:27 UT with 131 Å filter. Panel b: SOHO image from LASCO C2 taken at 20:48 UT. Panel c: PROBA-2 SWAP image taken at 07:40 UT on 15 October 2014. Panel d: STEREO-A SECCHI image at 21:39 UT using 195 Å filter. Panel e: GCS model fits to the LASCO C3 image. Panel f (different temporal scale): PROBA-2/LYRA time series of solar radiation measured by the aluminum and zirconium filter channels. The red arrow in panels a, c and d indicates the CME source location. Note that STEREO-A is on the opposite side of the Sun from the Earth (Figure 1).

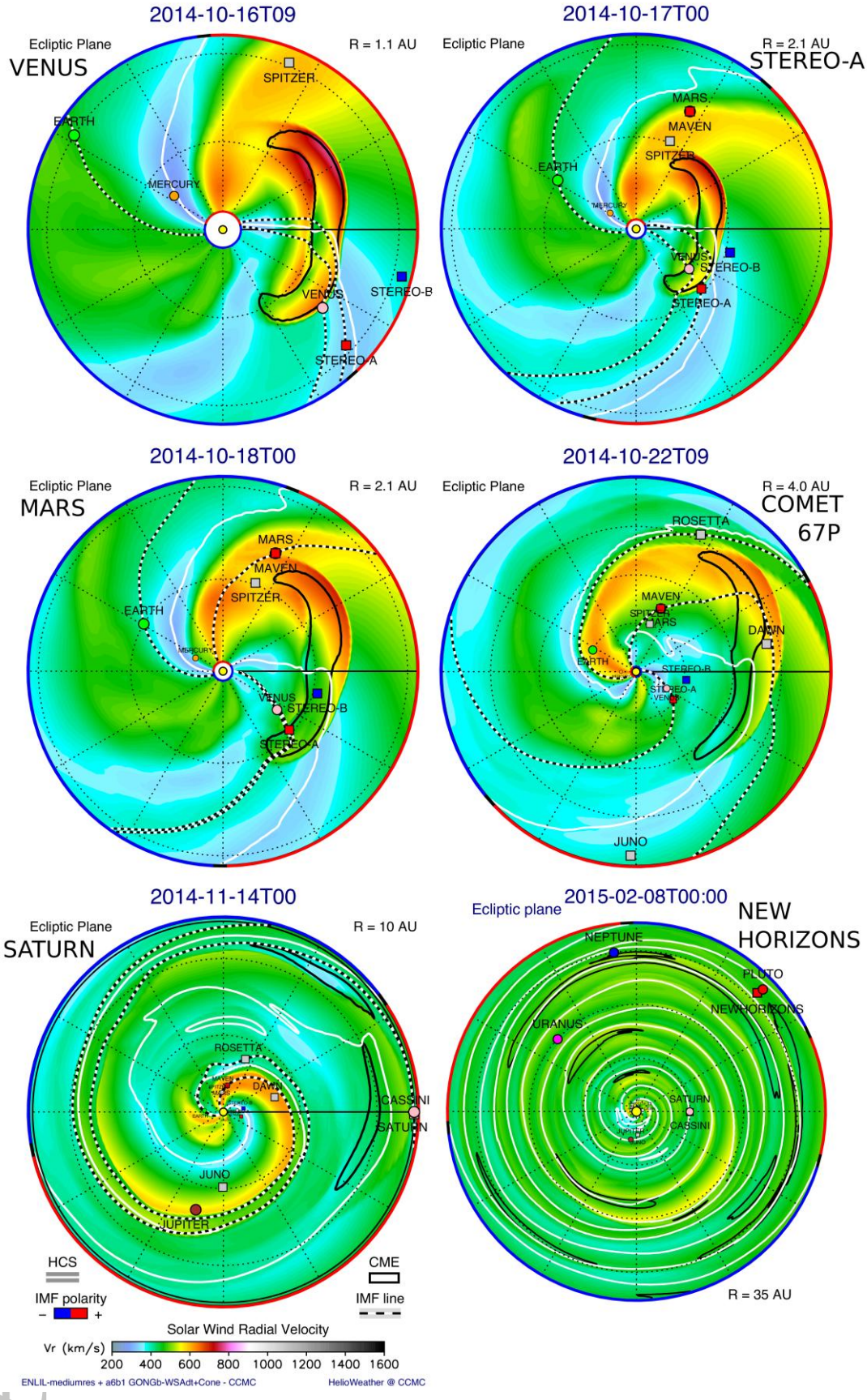

Figure 3: Stills of the solar wind velocity in the ecliptic plane from a WSA-ENLIL+Cone model simulation showing the ICME propagation, selected at the times of ICME closest approach to Venus, STEREO-A, Mars, comet 67P, Saturn and New Horizons. The full simulations are available at: http://ccmc.gsfc.nasa.gov; run numbers Leila_Mays_092716_SH_1, Leila_Mays_100116_SH_1. The colors represent the speed, as indicated in the color scale.

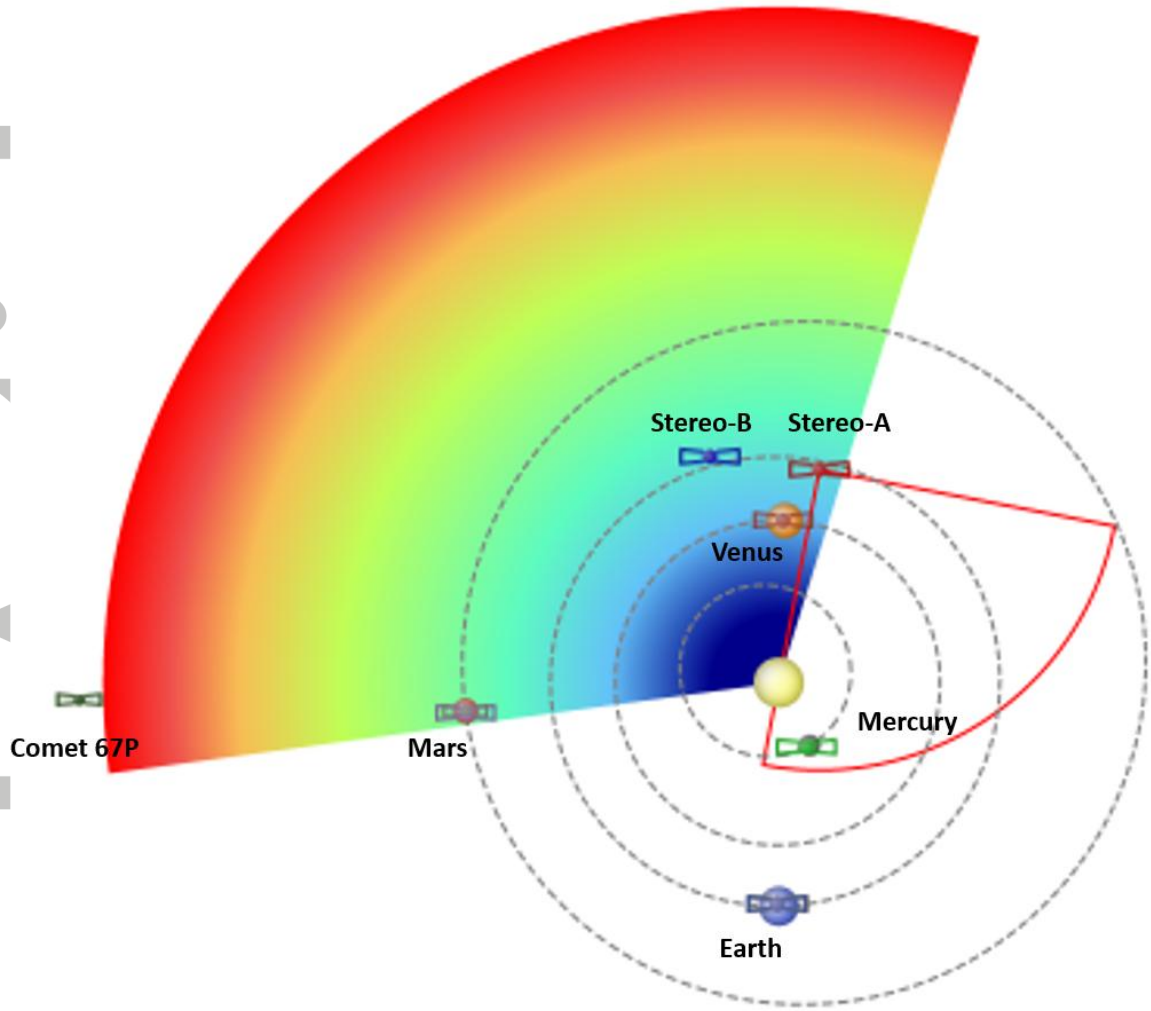

Figure 4: Output of the CDPP propagation tool. The ICME in rainbow-colors is shown here until ~ 3AU (Rosetta and comet 67P are just outside, on the left side). This view shows the ICME hitting Venus, STEREO-A and –B, Mars and Rosetta. The extent of the CME was set to 116°, in order to be able to hit Mars on one side and STEREO-A on the other side. The red circular sector indicates by default the STEREO-A field of view. The color bar is an indication of the varying heliocentric distance.

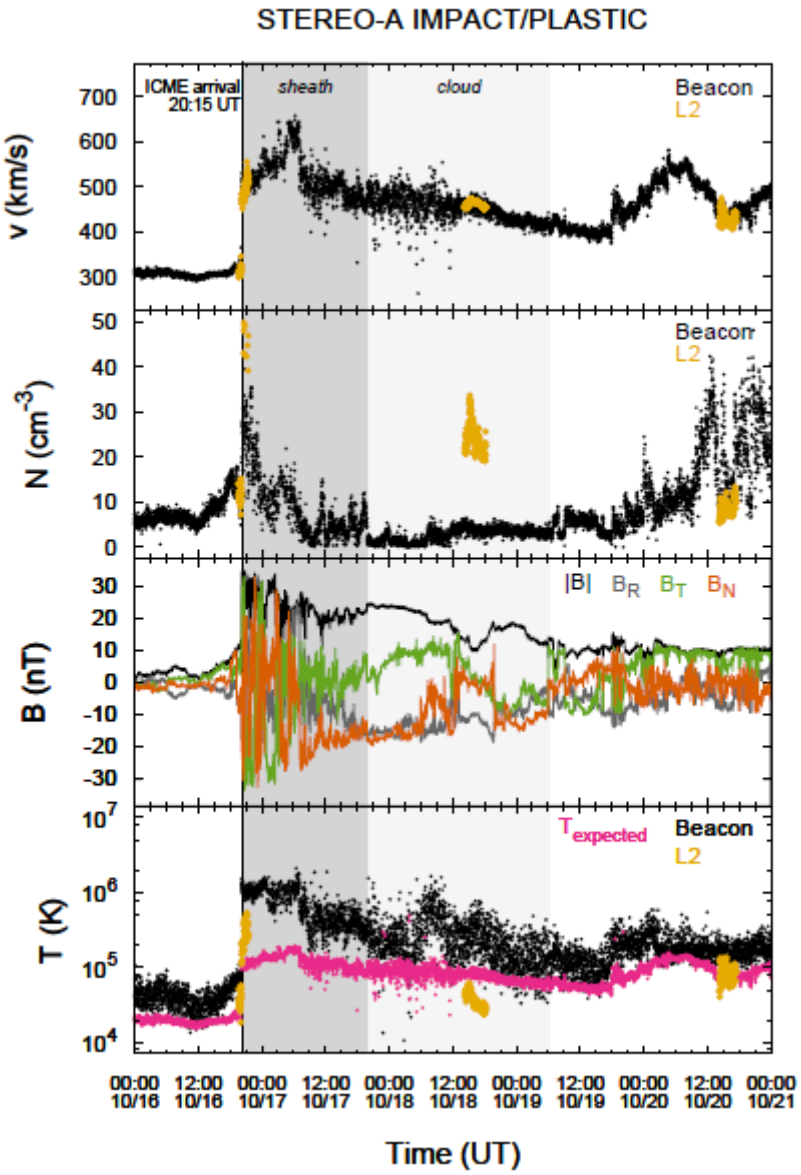

Figure 5: Solar wind observations of the shock (black vertical line) and ICME arrival at STEREO-A from the IMPACT/PLASTIC instruments. From top to bottom: Speed, density, magnetic field components in the RTN coordinate system, and temperature of the solar wind. "Beacon" stands for on-board processed beacon data which are not validated and are primarily intended for space weather near-time forecasting; "L2" stands for the 1D Maxwellian Level 2 data (in yellow) which have been validated and are processed on the ground using data with high statistics and low dead times. "Tex" stands for the expected temperature (in magenta).

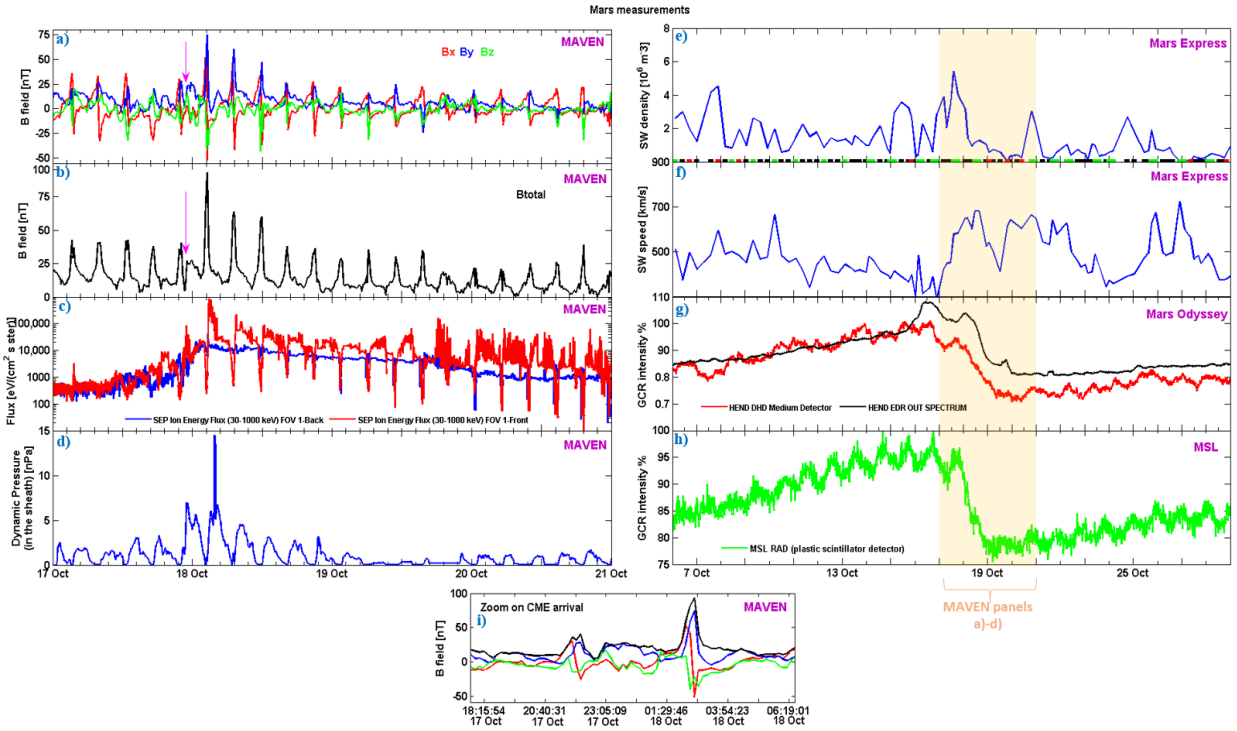

Figure 6: Observations of the shock/ICME arrival at Mars as detected by Mars Express, MAVEN, MSL and Mars Odyssey. Note that the time scales of panels a-d and panels e-h are different to give the best possible display of each dataset. Panels a and b: Components and magnitude of the magnetic field from MAVEN. The periodic peaks correspond to the periapsis of its orbit. Panel c: Ion Flux of SEP (30-1000 keV) from MAVEN. Panel d: Dynamic pressure estimated from MAVEN. All the MAVEN data come from the magnetosheath since the spacecraft was not in the Solar wind during this time. Panels e and f: Density and speed of the Solar wind respectively measured by Mars Express purely in the Solar wind. The color code along the abscises shows data flags (applicable to both panels), where black stands for no identified issues, red for bad fit likely due to EUV contamination, and green for when the ASPERA-3 IMA instrument was running in a badly suited post-acceleration level. Panel g: High energy neutrons flux for a proxy of the GCR intensity measured by Mars Odyssey in orbit around Mars. Two channels have been plotted, the Outer Scintillator (an anti-coincidence detector) in channels 9-16 (black) and the Derived HEND Data (DHD, red) in which a time-dependent correction has been applied to study only neutrons coming from Mars and not produced at the spacecraft. Both datasets have been normalized with respect to the highest DHD value (at the onset event) in the interval of the figure to compare with the percentage level of variation in GCR. Panel h: neutron detection as a proxy for the GCR intensity measured by the MSL on the surface of Mars. The green profile corresponds to data from a plastic detector which works as an anti-coincidence shield

in the energy range 10-100 MeV. Panel i: Zoom in on MAVEN magnetic field data (panels a and b together) at the arrival time of the ICME at Mars, to facilitate identification of the time of the ICME arrival (Table 1). The arrow indicates the ICME arrival.

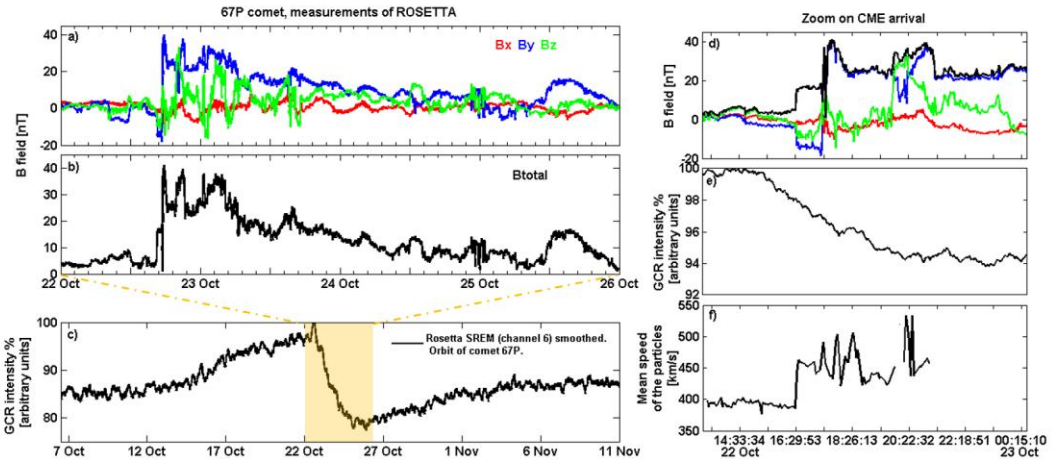

Figure 7: Observations of the ICME arrival at comet 67P by Rosetta. Panels a and b: Components and magnitude of the magnetic field respectively, in CSEQ-coordinates. Panel c: Rosetta SREM data (channel 6). Note that the temporal scale is larger in this panel. Panels d and e: Zoom on the magnetic field (panels a and b together) and radiation data (panel c) at the arrival time of the ICME at comet 67P. Panel f: Proton speed measured by the ICA sensor.

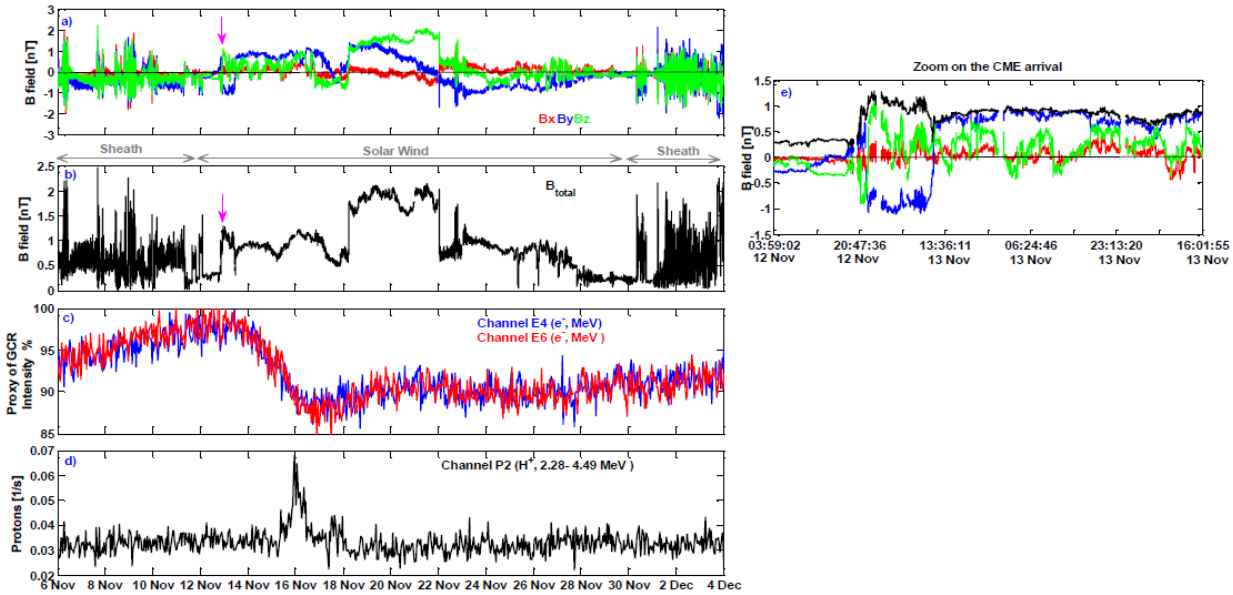

Figure 8: Observations of the shock and ICME arrival at Saturn by the Cassini spacecraft. Panels a and b: Components and magnitude of the magnetic field respectively. Panel c: Proxy for the GCR, obtained from the E4 and E6 channels of the LEMMS sensor. Panel d: Proxy for the GCR, from the LEMMS proton channel with energy 2.4-4.2 MeV. Panel e: Zoom on the magnetic field data (panels a and b together) to facilitate the identification of the arrival time of the ICME at Saturn (Table 1).

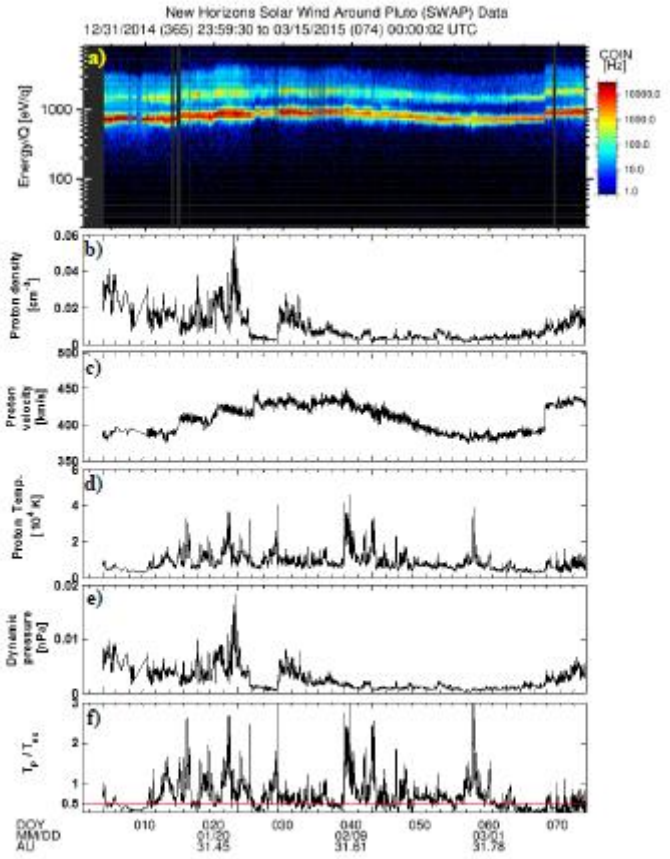

Figure 9: New Horizons SWAP data. Panel a: Ion spectrogram, with the top and bottom traces representing alpha particles and protons respectively. Panels b-f: Solar wind density, speed, temperature, dynamic pressure and ratio between the proton temperature and the expected temperature, as a possible ICME indicator [Elliott et al., 2012]. When that ratio is below 0.5, the interval could be an ICME. The period covers the first 80 days of 2015.

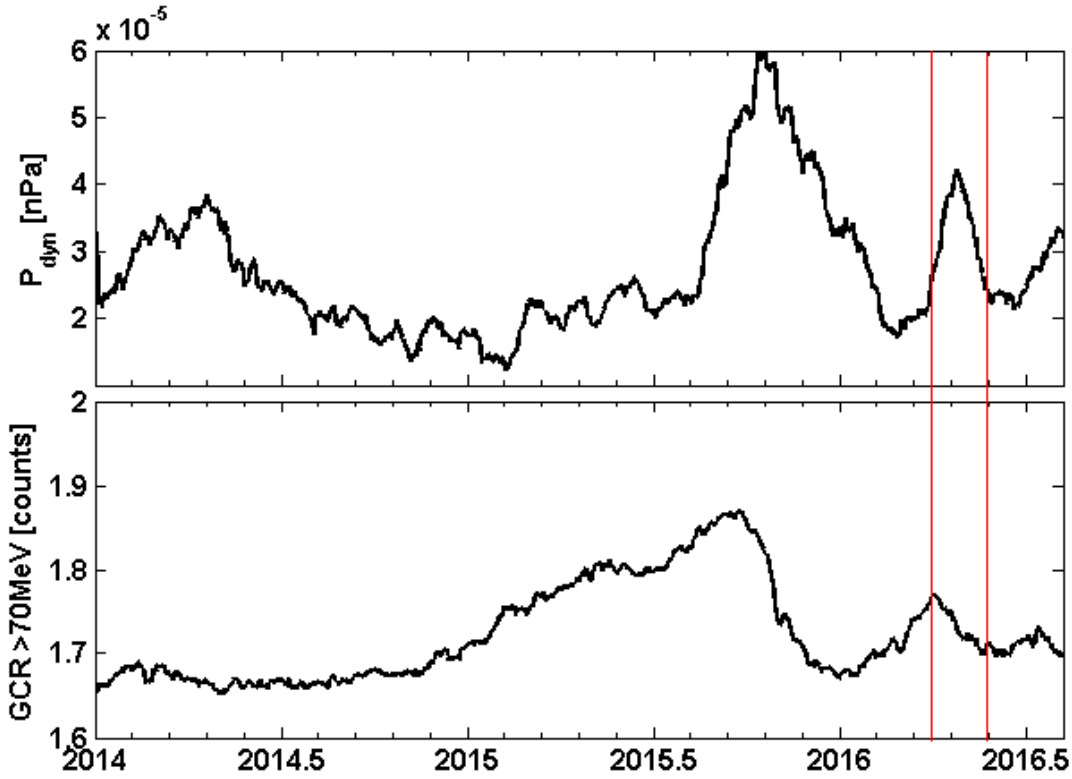

Figure 10: Voyager-2 data from 2014 to mid-2016 within the heliosheath. The upper panel shows the measured dynamic pressure while the bottom panel shows the GCRs with energies higher than 70 MeV. The two red vertical bars denote the event related to the ICME.

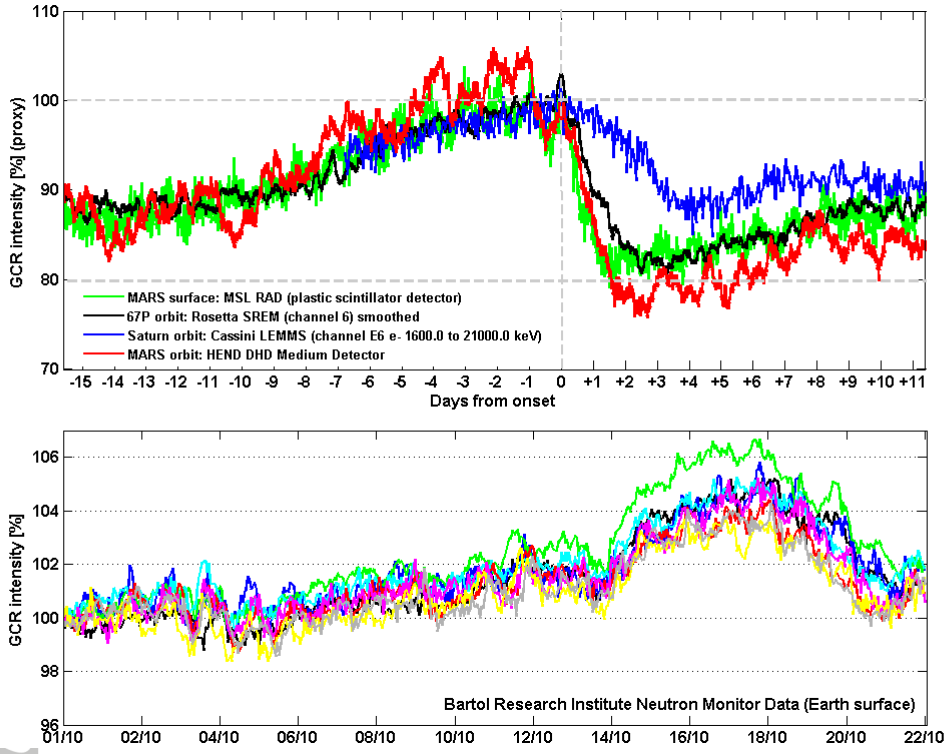

Figure 11: Top panel: Forbush decrease comparison between Mars in orbit (red), Mars at the surface (green), comet 67P in orbit (black) and Saturn in orbit (blue). The data were normalized for a better comparison of the relative decreases, expressed in percent change from the intensity immediately preceding the decrease. The onset (time zero on the abscissa) corresponds to the ICME ejecta passage at each location. Bottom panel: Neutron detection as a proxy for GCR at the Earth's surface at 8 different locations, i.e., McMurdo-Antarctica (LAT 77.9°S, LON 166.6°E) in black, Swarthmore-Pennsylvania/Newark-Delaware (LAT 39.9°N / 39.7°N, LON 75.4°W / 75.7°W) in blue, South Pole-Antarctica (LAT 90°S) in green, Thule-Greenland (LAT 76.5°N, LON 68.7°W) in light blue, Fort Smith- Canada (LAT 60.0°N, LON 111.9°W) in red, Peawanuck-Canada (LAT 55.0°N, LON 85.4°W) in magenta, Nain-Canada (LAT 56.5°N, LON 61.7°W) in yellow, and Inuvik-Canada (LAT 68.4°N, LON 133.7°W) in grey.

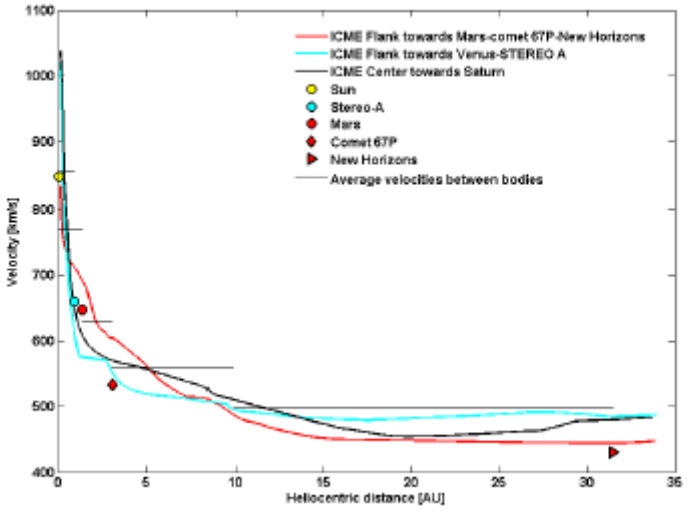

Figure 12: Simulated and observed solar wind speeds at several locations. The speed at the Sun is obtained from LASCO observations, and the New Horizons speeds are Solar wind speed observations taken around the estimated arrival time. The three profiles indicate the speed of the center and of both ICME flanks derived from the WSA-ENLIL+Cone simulations. The symbols denote the measured speeds at each location and the color-codes are the same as the color of the simulation curve that crosses each body. Average speeds between the solar system bodies encountered by the ICME are represented with a horizontal black line. For example, the average speed is 560 km/s between 3.1 and 9.9 AU, as indicated in Table 4.

Tables

Table 1: ICME propagation timeline

		Date and time [UT]	Heliocentric distance [AU]
Sun	Launch of the CME	14 OCT 2014 T18:30	
Venus	Putative arrival time from Venus Express housekeeping data	16 OCT 2014 T07:19	0.72
	CME associated shock/compression from WSA-ENLIL+Cone	16 OCT 2014 T09:00	
	CDPP propagation tool prediction	16 OCT 2014 T07:12	
STEREO-A	STEREO-A shock detection	16 OCT 2014 T20:00	0.96
	CME associated shock/compression from WSA-ENLIL+Cone	17 OCT 2014 T00:00	
	CDPP propagation tool prediction	16 OCT 2014 T20:57	
Mars	CME detection with Mars Express ASPERA data	17 OCT 2014 T15:45-22:50	1.41
	CME detection with MAVEN magnetometer data	17 OCT 2014 T22:53	
	FD onset with MSL RAD data (Plastic detector)	17 OCT 2014 T20:09	
	FD onset with HEND Mars Odyssey (DHD medium detector)	17 OCT 2014 T18:15	
	CME associated shock/compression from	18 OCT 2014 T00:00	

	WSA-ENLIL+Cone		
	CDPP propagation tool prediction	17 OCT 2014 T22:51	
Comet 67P	CME detection with Rosetta magnetometer data	22 OCT 2014 T16:30	3.13
	CME detection with Rosetta ion data (Solar wind proton energy)	22 OCT 2014 T17:24	
	FD onset with Rosetta SREM data (Channel 6)	22 OCT 2014 T14:24	
	CME associated shock/compression from WSA-ENLIL+Cone	22 OCT 2014 T09:30	
	CDPP propagation tool prediction	22 OCT 2014 T17:00	
Saturn	CME detection with Cassini-Huygens magnetometer data	12 NOV 2014 T18:55	9.94
	FD onset with Cassini-Huygens MIMI data	12 NOV 2014 T17:30	
	CME associated shock/compression from WSA-ENLIL+Cone	15 NOV 2014 T12:00	
	CDPP propagation tool prediction	12 NOV 2014 T16:09	
New Horizons	Time window based on solar wind speed (see text)	18 JAN-14 FEB 2015	31.49
	Possible detection of the ICME in the SWAP data	21-29 JAN 2015	
	CME associated shock/compression from	8 FEB 2015	

	WSA-ENLIL+Cone, prediction for the distance of NH (see text)		
	CDPP propagation tool prediction for 31.5 AU	24 JAN 2015	
Voyager 2	Possible MIR detection in the dynamic pressure and GCR data sets	Late March 2016	111.06

Table 2: Characteristics of the Forbush decreases at Mars, comet 67P, and Saturn. Data: MSL RAD data (E sensor). HEND DHD medium detector. Rosetta SREM Channel 6. Cassini-Huygens MIMI channel E6.

		Possible shock (start of the sheath passage) [UT]	Start of the ICME ejecta passage (CME plasma body) [UT]	End of the Forbush decrease [UT]	Magnitude of decrease (related to the ICME body) [%]	Duration of the decrease [hours]	Slope of the decreases [% / hour]
Mars	**MSL**	16 OCT 2014 T18:11	17 OCT 2014 T20:09	19 OCT 2014 T04:56	19	~33	0.57
	Mars Odyssey	16 OCT 2014 T18:05	17 OCT 2014 T18:15	19 OCT 2014 T08:35	23	~38.5	0.60
Comet 67P		22 OCT 2014 T09:50	22 OCT 2014 T14:24	25 OCT 2014 T02:40	17	~60	0.28
Saturn		12 NOV 2014 T18:30	15 NOV 2014 T10:30	16 NOV 2014 T21:20	15	~98.5	0.15

Table 3: Observed background solar wind speeds, and observed and modeled ICME speeds and at several locations. The solar ejection speed is obtained from a CGS fit to SOHO LASCO and STEREO A coronagraph observations, and the New Horizons solar wind speed is as observed around the possible ICME arrival time (DOY 021-029 2015).

Location	**Heliocentric distance [AU]**	**Measured background solar wind speed [km/s]**	**Measured ICME speed [km/s]**	**Modeled ICME speed with WSA-ENLIL+Cone model [km/s]**
Solar ejection	~0	Not available	850±200 at $21.5R_{\odot}$.	1015
Venus	0.72	Not available	Not available	625
STEREO-A	0.96	300	660	550
Mars	1.41	450-500	647	625
Comet 67P	3.13	400	550	500
Saturn	9.94	Not available	Not available	500
New Horizons	31.49	380-400	420-450	450

Table 4: Mean speed between two successive locations, based on timing of shock/ICME encounters. The New Horizons parameters are taken around the possible arrival time.

Segment	**Travel distance [AU]**	**Travel time [days]**	**Mean speed [km/s]**
Sun – STEREO-A	0.96	2.06	660
Sun – Mars	1.41	3.17	770
Mars – comet 67P	1.72	4.73	630
Comet 67P – Saturn	6.81	21.10	560
Saturn – New Horizons	21.55	74	504